


THE FLORIDA STATE UNIVERSITY
COLLEGE OF ARTS AND SCIENCES

THE SEASONAL VARIABILITY IN A MODEL
OF THE TROPICAL PACIFIC

by
Antonio J. Busalacchi Jr.

A Thesis submitted to the
Department of Oceanography
in partial fulfillment of the
requirements for the degree of
Master of Science

Approved:




Professor Directing Thesis











Chairman, Department of Oceanography

March, 1980

ABSTRACT

A simple linear model of the tropical Pacific Ocean is used to simulate the oceanic response to time-dependent wind stress forcing. A linear, one-layer, reduced-gravity transport model on an equatorial beta-plane is incorporated. The non-rectangular model basin extends from 18°N to 12°S . Bottom topography, thermohaline and thermodynamic effects are neglected.

The equatorial response, particularly at the eastern boundary, is studied along the same lines as Kindle. Annual and semiannual harmonics of the zonal equatorial wind stress calculated by Meyers are used to force the model. The east-west slope of the model pycnocline is compared with depth observations of the 14°C isotherm. The linear model generates a semiannual eastern boundary response remote from any region with strong second harmonics of the zonal wind stress. This response supports Meyers' hypothesis that at the eastern boundary the semiannual displacement of the thermocline is due to remote forcing.

The major application of the model is forced by mean monthly wind stresses based on 10 years of observations over the tropical Pacific. The resulting meridional profile of the pycnocline depth is a duplicate of Wyrcki's profile of dynamic height. The equatorial system of troughs and ridges is evident in the pycnocline profile. The seasonal variation of Wyrcki's profile of dynamic height. The equatorial system of troughs and ridges is evident in the pycnocline profile. The seasonal variation

of the major equatorial surface currents is compared with the observations. An annual Rossby wave emanating from the eastern boundary is found to modify the location and variability of the Countercurrent Trough. The current structure in the eastern equatorial Pacific agrees with Tsuchiya's dynamic topography maps of this region.

The results of the two model applications indicate that the dynamics inherent in linear theory are capable of reproducing the major features of the equatorial response and those of the equatorial current system.

ACKNOWLEDGEMENTS

This work was supported by the Division of Atmospheric Sciences, National Science Foundation, under Grant ATM7920485, the CUEA Project of IDOE, NSF and the Office of Naval Research. Computations were performed on the CDC Cyber 74 at the Florida State University, and the CDC 7600 at the National Center for Atmospheric Research. NCAR is supported by the National Science Foundation.

It is with a great deal of enthusiasm that I thank Dr. James J. O'Brien for his suggestion of this thesis topic. His support and guidance are deeply appreciated. I am also grateful of the time taken by Drs. Steven Blumsack, Richard Iverson and Raymond Staley while serving on my thesis committee. This research could not have been accomplished without the wind stress data provided by Drs. Klaus Wyrтки and Gary Meyers.

To my colleagues in the Mesoscale Air-Sea Interaction Group. I would like to express my gratitude for their comments and criticisms on this work. The long hours of drudgery provided by all those involved in the subjective analysis of the wind stress data is cheerfully acknowledged. I am also deeply indebted to Dr. John Kindle for his previous work and for the knowledge and friendship he has extended to me.

I wish to thank Susan Finney for typing most of the early draft copies and the final version of this thesis. I am very appreciative of the

I wish to thank Susan Finney for typing most of the early draft copies and the final version of this thesis. I am very appreciative of the

assistance provided by Ms. Judy Estes, Mr. Dale Hawkins, Mrs. Sheila O'Brien, Ms. Noreen O'Malley and Mr. Dewey Rudd.

The support and encouragement of my parents and my wife, Connie, has not gone unnoticed. I sincerely thank them for their patience and enduring love.

TABLE OF CONTENTS

	Page
ABSTRACT.	ii
ACKNOWLEDGEMENTS.	iv
TABLE OF CONTENTS	vi
LIST OF TABLES.	vii
LIST OF FIGURES	viii
1. INTRODUCTION.	1
2. THE NUMERICAL MODEL	7
3. THE EQUATORIAL RESPONSE TO SEASONAL HARMONICS OF THE ZONAL EQUATORIAL WIND STRESS.	16
a. The East-West Slope of the Model Pycnocline.	19
b. The Seasonal Response in the Eastern Equatorial Pacific	23
c. Comparison with a Previous Study.	30
4. THE SEASONAL VARIABILITY IN THE EQUATORIAL CURRENT SYSTEM.	34
5. SUMMARY AND CONCLUSIONS	68
APPENDIX.	73
REFERENCES.	74

LIST OF TABLES

Table	Page
1. Remote and local forcing effects at the eastern boundary.	66

LIST OF FIGURES

Figure	Page
1. Comparison of model geometry with the tropical Pacific Ocean. The model basin extends from 18°N to 12°S and 126°E to 77°W. The dashed line represents an open boundary; all remaining boundaries are solid walls.	10
2. Staggered grid stencil used in the numerical model. Along meridional boundaries the zonal transports are evaluated. At the open boundaries the U, V and h variables are calculated . .	12
3. The annual and semiannual harmonic deviations about the mean for the zonal equatorial wind stress ($\text{Nm}^{-2} \times 10$) across the Pacific as derived by Meyers (1979b).	17
4. Comparison of model pycnocline depth at the equator (dashed line) and mean depth of the 14°C isotherm (solid line) for a scatter diagram of observations between 1°N and 1°S (scatter diagram from Meyers, 1979b)	20
5. Mean annual zonal wind stress across the model basin for the MASIG wind stress data for 1961-1970. Dashed contours indicate an easterly wind stress. Contour interval is .02 Nm^{-2}	22
6. The x-t section along the equator for (a) zonal velocity during year 4 and (b) the upper layer thickness (ULT). The contour interval is .05 m s^{-1} for (a) and 10 m for (b).	24
7. Comparison of the pycnocline height anomaly (PHA) at the eastern boundary (solid line) and the seasonal variation about the mean depth of the 14°C isotherm within the band 80°W to 100°W at the equator (dashed line from Meyers, 1979b). Depth variations in meters	26
8. Upper layer thickness over the eastern half of the model basin for the last nine months of year 4. Equatorially trapped Kelvin and Rossby waves are depicted. The y-scale has been expanded to facilitate inspection of the plots. The contouring interval is 2 m	28, 29
Kelvin and Rossby waves are depicted. The y-scale has been expanded to facilitate inspection of the plots. The contouring interval is 2 m	28, 29

Figure	Page
9. Same as Fig. 7 except the solid line represents (a) the linear solution and (b) the nonlinear solution for Kindle's numerical model in a rectangular basin (from Kindle, 1979)	31
10. Seasonal variation along the equator of the pycnocline depth as predicted by Kindle's nonlinear numerical model (from Kindle, 1979). The contour interval is 10 m	33
11. Meridional profile of dynamic height relative to 500 db zonally averaged between 140°W and 170°E (from Wyrтки, 1974b).	36
12. Mean annual variation of sea level difference across the North Equatorial Current (A) and the Countercurrent (B) (from Wyrтки, 1974b)	38
13. Meridional profile of model pycnocline depth zonally averaged between 140°W and 170°E.	41
14. Pycnocline depth difference across the North Equatorial Current.	44
15. North Equatorial Current zonal velocity averaged between 140°W and 170°E.	45
16. Pycnocline depth difference across the North Equatorial Countercurrent.	46
17. North Equatorial Countercurrent zonal velocity averaged between 140°W and 170°E.	47
18. Pycnocline depth difference across the South Equatorial Current	48
19. South Equatorial Current zonal velocity averaged between 140°W and 170°E.	49
20. Pycnocline depth beneath (a) the Countercurrent Trough and (b) Equatorial Ridge	51
21. Seasonal variation of (a) sea level difference between Pago Pago and Canton and (b) surface current between Canton and Samoa (from Wyrтки, 1974a)	52
22. Upper layer thickness over the eastern half of the model basin during year 4. The y-scale has been expanded to facilitate inspection of the plots. The contouring interval is 10 m . . .	55, 56
23. Upper layer thickness over the entire model basin during year 4. The y-scale has been expanded to facilitate inspection of the plots. The contouring interval is 10 m . . .	55, 56
23. Upper layer thickness over the entire model basin during October. Contouring interval is 10 m.	57

Figure	Page
24. Zonal velocity flow field over the entire model basin during October. Contouring interval is $.1 \text{ m s}^{-1}$	60
25. Pycnocline height anomaly at the equatorial eastern boundary due to forcing of mean monthly wind stresses. Depth variations in meters.	62
26. Zonal equatorial wind stress (a) at the equatorial eastern boundary and (b) averaged between 160°W and 120°W	64

1. INTRODUCTION

In order to understand the circulation in the atmosphere and ocean it is necessary to understand how the ocean currents are affected by the overlying wind field. Heat exchange between the atmosphere and ocean is a primary driving force in the general circulation of the atmosphere. In the oceans the transport of heat is governed by major ocean currents. The surface ocean currents are coupled with the overlying wind field so that changes in wind stress result in fluctuations of the currents. Since the massive equatorial Pacific receives and stores large quantities of heat, the effect of the surface wind stress is very important in this region.

In the past 30 years there have been several studies estimating the wind stress fields in the Pacific, e.g., Scripps Institution of Oceanography (1948), Hidaka (1958), Hellerman (1967), and Wyrтки and Meyers (1975a, b; 1976). The data of Wyrтки and Meyers are the most complete set of Pacific wind stress estimates at the present time, yet their distribution still has regions with few or no wind stress observations. During 1978, the Mesoscale Air-Sea Interaction Group (MASIG), under Dr. James J. O'Brien, undertook the task of subjectively analyzing and eliminating the "holes" in Wyrтки and Meyers' data set. The MASIG analysis provides ten years of wind stress data on a 2° by 2° grid from 30°N to 30°S for ten years of wind stress data on a 2° by 2° grid from 30°N to 30°S for

the extent of the Pacific. This type of data base is very useful as the input for several numerical models of ocean circulation.

The inclusion of wind stress forcing in a model of ocean dynamics was first performed successfully by Sverdrup (1947). This work related the curl of the wind stress to the horizontal mass transport. Sverdrup's work was followed up and extended by Stommel (1948) and Munk (1950). These early studies created a demand for wind stress data over the oceans.

Additional studies have investigated the effect of surface wind stresses on vertical velocities. Yoshida (1955) accounted for variations in oceanic circulation with a model in which wind stress curl causes a vertical velocity that changes the meridional slope of the thermocline and likewise density surfaces. Meyers (1975) used this line of reasoning to show how changes in the depth of the thermocline in the central Pacific were in phase with geostrophic transport. Variations in the North Pacific Equatorial Current observed during the Trade Wind Zone Oceanography Study, February 1964 to June 1965, were reproduced by Meyers using the model originally developed by Yoshida (1955) and Federov (1961). Further work by Meyers (1978) demonstrated the effect of Ekman pumping and geostrophic divergence on the depth of the thermocline. An analytical model based on Ekman layer theory has been used by DeWitt and Leetmaa (1978) to compare predicted thermocline displacements and observed depth variations of the thermocline in the tropical North Pacific. White (1977, 1978) and Meyers (1978, 1979a) have addressed the existence of an annual baroclinic Rossby wave emanating from the eastern Pacific. White (1977, 1978) and Meyers (1978, 1979a) have addressed the existence of an annual baroclinic Rossby wave emanating from the eastern

boundary, propagating westward and modulating the seasonal response due to Ekman pumping in the tropical and midlatitude North Pacific.

A significant portion of our knowledge of the equatorial current-trade wind system is obtained from dynamic height and sea level analyses within the tropics. Reid (1961) has computed the geopotential anomaly relative to 1000 decibars over the Pacific Ocean based on a multitude of hydrographic observations. The resultant dynamic topography yielded a geostrophic expression of the major equatorial currents.

By using sea level observations taken at oceanic islands in the central and western Pacific, Wyrтки (1974a, b) was able to describe the seasonal characteristics of the equatorial currents in this region. The major findings were that variations in the North Equatorial Current and the North Equatorial Countercurrent are in phase and both tend to be weakest in spring and strongest in fall. The South Equatorial Current was found to be 180° out of phase with the Countercurrent and North Equatorial Current. In conjunction with determining the phase and amplitude relations of the equatorial currents, Wyrтки mapped out the dynamic topography of the western tropical Pacific based on data from hydrographic and sea level stations. By a series of troughs and ridges this dynamic topography marks the position of the major equatorial currents.

Another step forward in the study of the equatorial Pacific was the suggestion by Wyrтки (1975) that the onset of the El Niño phenomenon is the result of a remote equatorial Pacific response to changes in the overlying wind field. Wyrтки demonstrates that there is a buildup in the southeast trades in the central Pacific two years prior to an El Niño overlying wind field. Wyrтки demonstrates that there is a buildup in the southeast trades in the central Pacific two years prior to an El Niño event. When the winds relax, an equatorially trapped Kelvin wave may be

excited, thus providing a mechanism for the westward transport of warm water. This hypothesis was subsequently reinforced by the efforts of Hurlburt et al., (1976) and McCreary (1976). In the most recent model simulation of El Niño, Kindle (1979) uses a wind intensification-relaxation-intensification forcing sequence to reproduce the double-peak sea level signature found in observations along the eastern boundary during certain El Niño events.

A further topic of interest concerning the equatorial Pacific Ocean is the seasonal variability in the eastern tropical Pacific. Before we are able to fully understand the El Niño phenomenon, we must have a basic understanding of the seasonal signal in the eastern tropical Pacific; for it is certain intense perturbations of this seasonal signal that are termed El Niño. Two pertinent pieces of work regarding the seasonal response in the equatorial Pacific are those of Meyers (1979b) and Kindle (1979).

From observational data regarding the equatorial wind stress field and depth variations of the 14°C isotherm, Meyers demonstrates that there are large second harmonic variations in depth of the 14°C isotherm in the eastern equatorial Pacific. Meyers hypothesizes that this is a remote response to large second harmonics of the zonal wind stress over the central Pacific. As Meyers states, "It will be challenging and interesting to see if the main features of the annual variability can be reproduced by linear models (McCreary, 1976, 1977; Wunsch, 1977) which permit forced and free equatorial Kelvin and Rossby waves".

The wind stress means and harmonic coefficients that Meyers derived permit forced and free equatorial Kelvin and Rossby waves".

The wind stress means and harmonic coefficients that Meyers derived in his study may be conveniently used to force a numerical model of the

equatorial Pacific. Kindle did exactly that with a nonlinear model in a rectangular basin. The results from the numerical model yield a pycnocline height anomaly response (PHA) at the eastern boundary that is very similar to observations. A linear numerical model and a linear analytical model were used together to examine in detail the nonlinear seasonal variation at the equatorial eastern boundary. Kindle's analysis demonstrates that Kelvin waves emanating from the region of strong wind stress second harmonics together with their reflections as Rossby waves provide the major contributions to the PHA response at the eastern boundary.

The purpose of this study is to determine whether or not the physics inherent in linear theory are capable of reproducing the major features of the equatorial eastern boundary response and those of the equatorial current system. In order to analyze and investigate the seasonal response in the tropical Pacific, this paper will incorporate a one-layer, reduced-gravity, linear transport model on a β -plane. The first baroclinic equivalent depth (Lighthill, 1969) of the model is chosen to be 0.41 m. The choice of this model parameter is based on typical values for the density jump across the thermocline and depth of the thermocline in the equatorial Pacific. The coastline geometry of the model basin is an idealization of the Pacific Ocean from 18°N to 12°S. A non-rectangular model basin was chosen because the wind stress forcing used in one of the case studies is based on wind observations over the non-rectangular Pacific Ocean basin. An open boundary condition is applied at the northern and southern boundaries, enabling coastal Kelvin waves and Rossby waves to pass through without contaminating the interior solution.

The first application of the numerical model is one where the applied forcing is composed of the mean zonal wind stress and the annual and semiannual harmonics of the zonal wind stress about the equator as derived by Meyers (1979b). The salient features are 1) the east-west slope of the model pycnocline compared with observations of the thermocline slope, 2) the seasonal response in the eastern equatorial Pacific, 3) comparisons between the results of this linear numerical model and the nonlinear numerical simulations of Kindle (1979), and 4) comparison of the results of this model application with a subsequent model run forced by long-term mean monthly winds over the entire basin.

The second model application includes forcing by mean monthly wind stresses calculated from ten years of wind stress observations over the Pacific Ocean. Ten years (1961-1970) of the Wyrski and Meyers (1975a, b) wind stress data on a 2° latitude by 10° longitude grid have been subjectively analyzed onto a 2° by 2° mesh. This wind stress data was subsequently averaged over the ten year span to obtain a mean wind stress representative of each month in a year, evaluated at every grid point. The seasonal variability of the thermocline displacement and variability in the tropical Pacific current system is investigated. The depth of the model pycnocline is shown to be comparable with observations of the dynamic topography across the equatorial current system. The model results will show that local forcing together with remotely forced equatorial waves result in the seasonal variation of the equatorial currents and the seasonal response at the equatorial eastern boundary.

and the seasonal response at the equatorial eastern boundary.

2. THE NUMERICAL MODEL

A one-layer, reduced-gravity, linear transport model on an equatorial β -plane will be used to study the oceanic response to an applied wind stress forcing. This reduced-gravity formulation assumes the ocean to have a dynamically active, incompressible, hydrostatic, homogeneous upper layer. At the base of the upper layer a finite density jump exists, this interface being the location of the model pycnocline. In this model ocean it is assumed that at some depth beneath the upper layer the horizontal pressure gradient is zero. This assumption results in the elimination of the barotropic mode and the upper layer horizontal flow is then described by the gravest baroclinic mode. The reduced-gravity approach has been used often in recent models of tropical oceans (McCreary, 1977; Lin and Hurlburt, 1980; Adamec and O'Brien, 1978; Cane, 1979a, b; Kindle, 1979). Meyers (1979b) has shown, using sea level and interfacial depth profiles, that the central Pacific and, during most of the year, the eastern Pacific, act in a manner compatible with the dynamics implicit in the reduced-gravity approach. The profiles show that variations in sea level and 14°C isothermal depth are 180° out of phase. This phase relation allows a zero pressure gradient to exist below the upper layer.

to exist below the upper layer.

The linear model equations for an equatorial β -plane are as follows:

$$\frac{\partial \vec{V}}{\partial t} = -\beta y \hat{k} \times \vec{V} - c^2 \nabla h + \frac{\vec{\tau}}{\rho} + A \nabla^2 \vec{V} \quad (1a)$$

$$\frac{\partial h}{\partial t} = -\nabla \cdot \vec{V} \quad (1b)$$

$$\vec{V} = U \hat{i} + V \hat{j} \quad (1c)$$

$$U = uH \quad V = vH \quad (1d)$$

where U , V are the respective x , y -components of the horizontal transport, c is the baroclinic phase speed taken to be $2. \text{ m s}^{-1}$, and the wind stress, $\vec{\tau}$, is included as a body force (Charney, 1955). The upper layer thickness is denoted by h . The initial thickness of the layer is H . The diffusive terms are included to bring the horizontal flow to zero along closed boundaries. Since this model is linear, if any mean or background flow field were to exist prior to the beginning of the model integration, the results of the model would simply be superimposed upon the mean state. The linear numerical model also has the advantage of being able to be compared with analytical models of the same problem. A right-handed Cartesian coordinate system is employed with x -positive eastward. A list of symbols and model parameters may be found in the Appendix. Bottom topography, thermohaline and thermodynamic effects have been neglected in the present model.

The model basin extends from 18°N to 12°S and 126°E to 77°W . The latitudinal extent was chosen to include the major equatorial currents, while attempting to keep computer storage low. The longitudinal extent encompasses the entire Pacific basin. Philander (1979) has demonstrated while attempting to keep computer storage low. The longitudinal extent encompasses the entire Pacific basin. Philander (1979) has demonstrated the necessity of having a large basin width. Since the wind stress

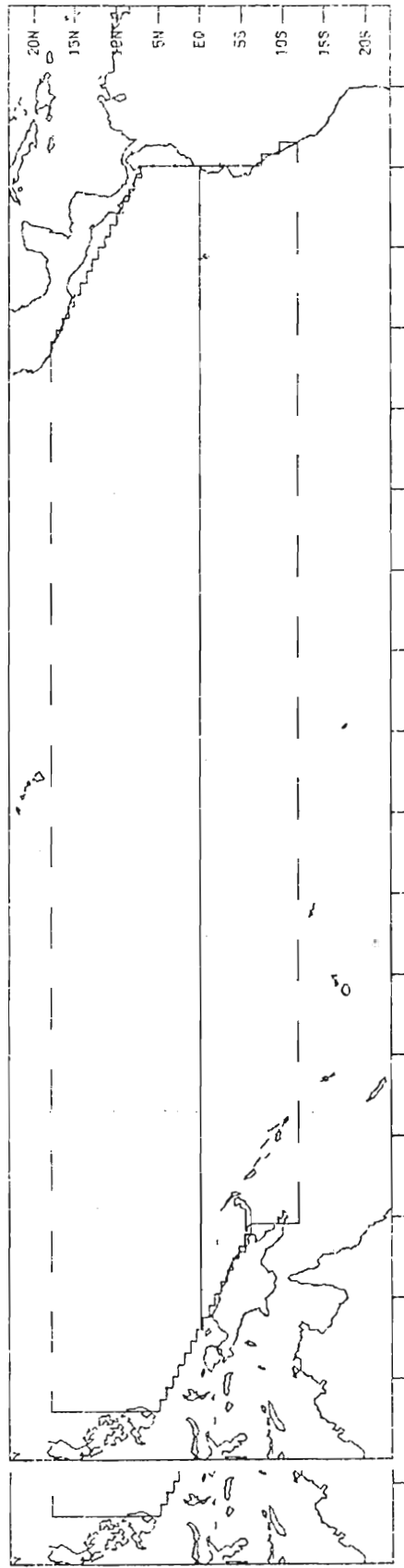
forcing to be used is derived from wind observations over the Pacific, it is important that the model basin approximate the coastline geometry of the Pacific Ocean. Boundary effects present at a given location in the wind field will then correlate with the model geometry. The coastline idealization chosen is shown in Fig. 1.

Meridional boundaries are taken to be solid walls. An open boundary condition is applied at the northern and southern boundaries permitting the passage of coastal Kelvin waves and Rossby waves, thus preventing the contamination of the interior solution. The open boundary condition is that of Hurlburt (1974), simplified for a reduced-gravity model (Kindle, 1979). This boundary condition provides an approximation for the longshore pressure gradient at a zonal boundary. The major assumptions used in the development of the boundary condition are that the meridional flow field is in nearly geostrophic balance and all longshore derivatives are negligible except for the pressure term in the V equation and the y-derivative in the continuity equation. For the present model, the boundary condition becomes:

$$\frac{\partial h}{\partial y} \Big|_x = \frac{1}{Y} (h \Big|_x - h \Big|_{x=0}) \quad (2)$$

where Y is the distance from the open boundary to the equator and $x = 0$ represents the western boundary. While some degree of smoothing is required at the boundary to suppress the "noise" level, this boundary condition does in fact allow coastal Kelvin waves and Rossby waves to pass through. A severe test of the boundary condition occurred during a trial run of the model when a point in the interior region height pass through. A severe test of the boundary condition occurred during a trial run of the model when a point in the interior region height field was changed by 10 orders of magnitude. The resulting large amplitude gravity waves passed directly through the open boundaries.

MODEL GEOMETRY



130 130E 140E 150E 160E 170E 180 170W 160W 150W 140W 130W 120W 110W 100W 90W 80W 70W

Fig. 1. Comparison of model geometry with the tropical Pacific Ocean. The model basin extends from 18°N to 12°S and 126°E to 77°W. The dashed line represents an open boundary; all remaining boundaries are solid walls.

The model grid size is 40 km in both x and y. This grid size gives the model a scale of resolution at or smaller than the equatorial and coastal radii of deformation. A staggered grid is used to reduce computer core storage (Fig. 2). A two hour time step is incorporated by the model. This combination of grid size and time step is well within the constraints posed by the C-F-L condition. The model equations are integrated over a period of four years. This provides sufficient time for most of the initial transients to die out and for a seasonal signal to set up.

All time derivatives are handled explicitly by a leap-frog scheme. The Coriolis terms are centered in time and averaged in space. All single derivatives in space are replaced by standard second-order centered differences. The diffusive terms are treated using the Dufort-Frankel scheme. The model equations are forward differenced in time every five days to prevent time splitting.

To gain an insight into the dynamics present in this model, Eq. (1) will be briefly analyzed. This discussion will be restricted to the model interior so that the diffusive terms may be neglected. The oceanic response to a time varying wind stress will consist of geostrophic currents and various wavelike signals. The homogeneous solution to Eq. (1) represents three types of waves; dispersive and non-dispersive Rossby waves, mixed Rossby-gravity waves and inertia-gravity waves (Moore and Philander, 1977).

The physics away from the equator ($>5^\circ$) allow the following solutions. For low frequency forcing, the horizontal momentum equation is:

The physics away from the equator ($>5^\circ$) allow the following solutions. For low frequency forcing, the horizontal momentum equation is:

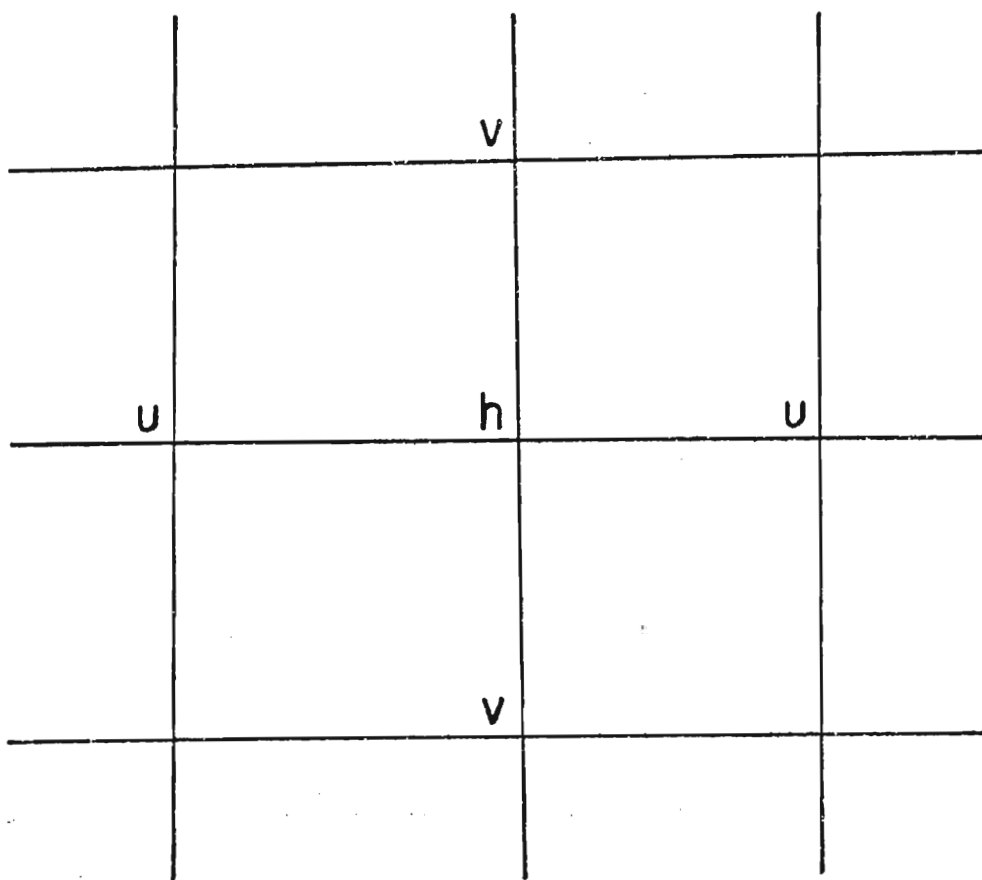


Fig. 2. Staggered grid stencil used in the numerical model. Along meridional boundaries the zonal transports are evaluated. At the open boundaries the U, V and h variables are calculated.

$$\beta y \hat{k} \times \vec{V} = -c^2 \nabla h + \frac{\vec{\tau}}{\rho} . \quad (3)$$

The momentum and continuity equations may be combined to form a single equation for the meridional transport:

$$c^2 \beta V_x - \beta^2 y^2 V_t = c^2 \hat{k} \cdot (\nabla \times \frac{\vec{\tau}}{\rho})_x + \beta y (\frac{\tau_x}{\rho})_t \quad (4)$$

(c.f., McCreary, 1977). Non-dispersive Rossby waves are the only free wave response to this equation. For latitudes much greater than the radius of deformation, $(\frac{c}{\beta})^{\frac{1}{2}}$, the phase speed and group speed of these waves is $c_R = \frac{c^2}{\beta y^2}$ (Lighthill, 1969).

The vertical displacement of the pycnocline may be analyzed by forming the vorticity equation (Meyers, 1978). Taking the curl of Eq. (1a) and substituting for the divergence term in Eq. (1b) yields:

$$\frac{\partial h}{\partial t} = \frac{V}{y} - \frac{\hat{k}}{\beta y} \cdot \nabla \times \frac{\vec{\tau}}{\rho} = \frac{c^2}{\beta y^2} h_x - \hat{k} \cdot \nabla \times \frac{\vec{\tau}}{\rho \beta y} . \quad (5)$$

The first term is the vortex stretching term or the temporal change in depth of the pycnocline. The second term represents the vertical velocity generated by the divergence of the meridional transport due to the β -effect. This term can be expanded to demonstrate that a negative zonal pressure gradient (fourth term) will result, via geostrophy, in an upwelling velocity. The third and fifth terms are similar expressions describing the change in angular momentum of the fluid due to the wind stress curl. The Rossby wave solution to the model equations is contained in the fourth term of Eq. (5). Therefore, the vorticity equation may be interpreted as consisting of a local response (wind stress contained in the fourth term of Eq. (5)). Therefore, the vorticity equation may be interpreted as consisting of a local response (wind stress curl) and a westward propagating Rossby wave response (Lighthill, 1969; White, 1977; Meyers, 1979a).

For long period forcing, the extraequatorial region is in equilibrium when the time derivative in Eq. (5) becomes small. The steady state that occurs is the baroclinic Sverdrup balance,

$$\beta V = \hat{k} \cdot \nabla \times \frac{\vec{\tau}}{\rho} . \quad (6)$$

This occurs after the long, non-dispersive Rossby waves generated at the eastern boundary have passed through the interior (White and McCreary, 1974). For the model studied here, it would take $1\frac{1}{2}$ - 10 years for the entire basin to achieve a Sverdrup balance.

The dynamical response at the equator ($\pm 5^\circ$) is unique because of the breakdown of the Coriolis force. For time scales long enough such that high frequency inertia-gravity waves may be neglected, the governing equations yield a single expression in V :

$$V_{yyt} - \frac{\beta^2 y^2}{c^2} V_t + \beta V_x = \hat{k} \cdot (\nabla \times \frac{\vec{\tau}}{\rho})_x + \frac{\beta y}{c^2} (\frac{\tau^x}{\rho})_t - \frac{1}{c^2} (\frac{\tau^y}{\rho})_{tt} . \quad (7)$$

The homogeneous solution to this equation admits dispersive and non-dispersive baroclinic Rossby waves (McCreary, 1977).

A further equatorial wavelike solution is permitted when the meridional transport is constrained to zero. The resulting solution is that for the equatorially trapped Kelvin wave (Moore and Philander, 1977). This is an eastward propagating, non-dispersive wave with phase speed, $c = (g'H)^{\frac{1}{2}}$. The trapping distance is the equatorial radius of deformation.

The numerical results of Cane (1979b) have shown that for steady zonal winds the near equatorial region achieves equilibrium after the

The numerical results of Cane (1979b) have shown that for steady zonal winds the near equatorial region achieves equilibrium after the passage of the initial Kelvin wave and first reflected Rossby wave.

After that point in time all wind stress energy goes into balancing the pressure gradient:

$$c^2 h_x = \frac{\tau^x}{\rho} . \quad (8)$$

Since equatorially trapped waves quickly propagate across the basin (15,000 km), this balance would be achieved on the order of one year. It must be remembered that the sudden application of a steady forcing results in solitary wave disturbances. On the other hand, periodic forcing results in the continuous generation of waves.

3. THE EQUATORIAL RESPONSE TO SEASONAL HARMONICS OF THE ZONAL EQUATORIAL WIND STRESS

Two recent studies have investigated the seasonal variability in the eastern equatorial Pacific Ocean. Meyers (1979b) has analyzed equatorial bathythermographic data to arrive at his findings. Kindle (1979) uses a nonlinear numerical model to corroborate the ideas set forth by Meyers.

On the basis of all bathythermographic data on file at the National Oceanographic Data Center for the Pacific Ocean from 2°N to 2°S, Meyers has computed the mean depth and the first and second harmonic variations in depth of the 14°C isotherm. The data were analyzed in seven, 20° wide, longitudinal bands ranging westward from 80°W to 140°E. The 14°C isotherm was chosen for analysis because it is representative of vertical variations in depth of the bottom of the thermocline. Annual and semiannual harmonics were also calculated for the zonal wind stress over the same longitudinal bands (Fig. 3). Meyers found evidence suggesting remote forcing as a possible mechanism operating in the eastern Pacific. His work demonstrates that the 14°C isotherm exhibits strong second harmonic variations in depth in the eastern Pacific, while strong second harmonics of zonal wind stress are only evident in the central Pacific (180° to 120°W).

One of Kindle's main objectives was to test the remote forcing (180° to 120°W).

One of Kindle's main objectives was to test the remote forcing hypothesis proposed by Meyers. Kindle used the mean zonal wind stress

ZONAL WIND STRESS

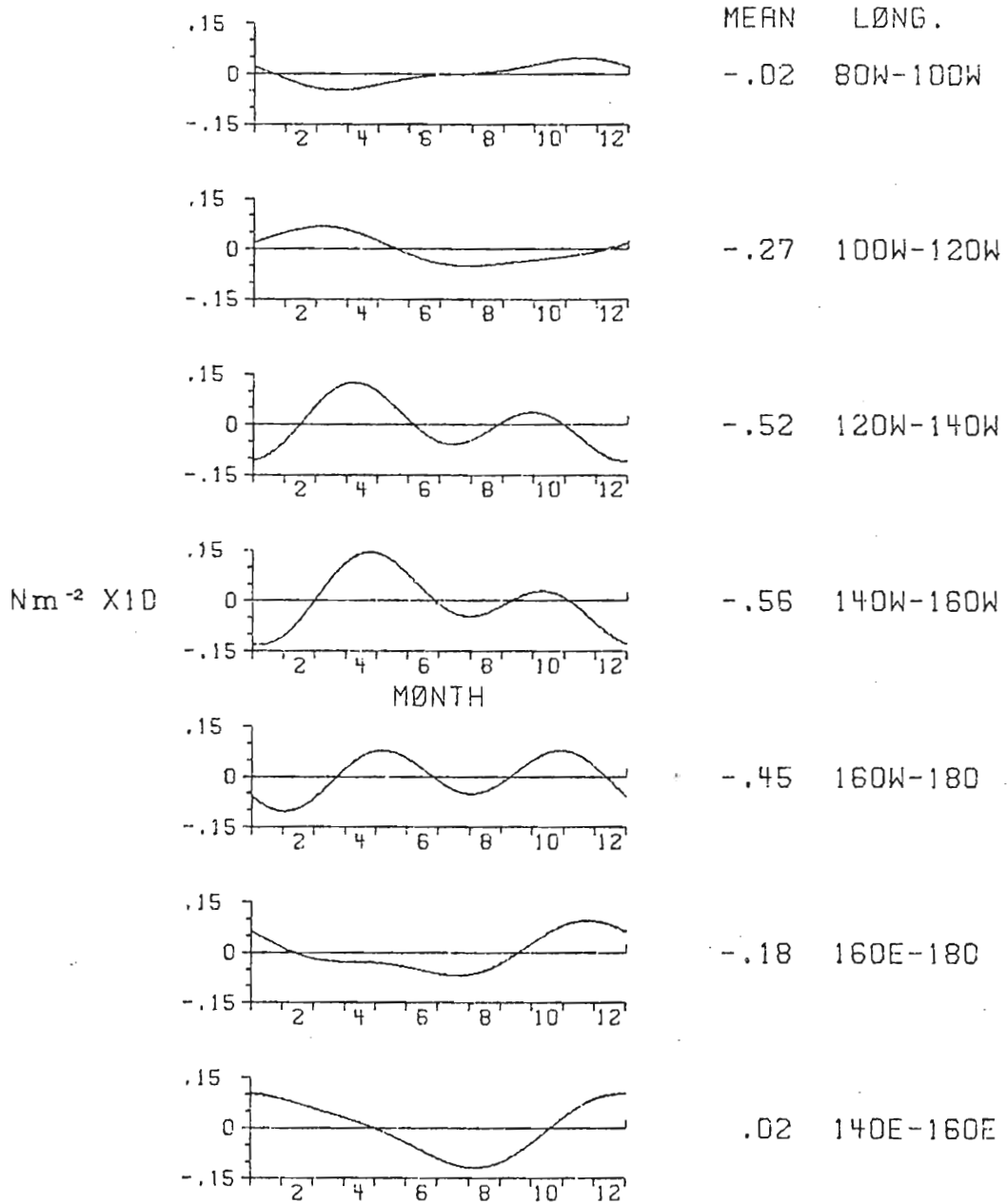


Fig. 3. The annual and semiannual harmonic deviations about the mean for the zonal equatorial wind stress ($Nm^{-2} \times 10$) across the Pacific as derived by Meyers (1979b).

Fig. 3. The annual and semiannual harmonic deviations about the mean for the zonal equatorial wind stress ($Nm^{-2} \times 10$) across the Pacific as derived by Meyers (1979b).

and the first and second harmonics of the zonal wind stress analyzed by Meyers, to force a nonlinear numerical model of the Pacific Ocean in a rectangular basin from 15°N to 15°S and 80°W to 144°E . Kindle's nonlinear model succeeded in producing a pycnocline height anomaly (PHA) response for the eastern boundary at the equator, similar in phase and amplitude to Meyers' observed semiannual (second harmonic) signal for the vertical displacement of the 14°C isotherm. An analytical model which isolates the individual effects of different trapped equatorial internal waves was employed by Kindle. He determined that the semiannual response in the eastern tropical Pacific was due to equatorially trapped Kelvin waves generated in the central equatorial Pacific, thus strengthening Meyers' remote forcing hypothesis. Kindle also demonstrated that the equatorial east-west slope of the model pycnocline is in agreement with the observed slope of the thermocline.

In our first case study using the numerical model described in section 2, the wind stress forcing is composed of the mean zonal wind stress and the annual and semiannual harmonics as calculated by Meyers. The zonal wind stress is applied in seven 20° wide longitude bands which encompass the range from 80°W to 140°E . In the small remaining areas near the boundaries, the wind stress is zero. Although these winds were calculated from observations $\pm 2^{\circ}$ about the equator, the magnitude of this wind stress, unique to each band, is extended uniformly to the northern (18°N) and southern (12°S) boundaries. Zonally, within each band, the wind stress is invariant. If we confine our attention to the equatorial response, one may take the liberty of extending equatorial band, the wind stress is invariant. If we confine our attention to the equatorial response, one may take the liberty of extending equatorial winds to the boundaries, since changes in the wind stress outside the

equatorial radius of deformation ($\pm 3^\circ$) have little or no effect on the equatorial response (McCreary, 1976). Divergences along the edge of each wind stress band will be capable of generating Rossby waves and equatorially trapped Kelvin waves. Since no wind stress curl can be generated, a Sverdrup balance is impossible. This should lead to a steady state balance in which the wind stress is balanced by the zonal pressure gradient upon which the effects of equatorial waves have been superimposed.

The main objectives of this model application are a) to compare the east-west slope of the model pycnocline to observations of the thermocline slope, b) to duplicate the seasonal response in the eastern equatorial Pacific, and c) to compare the results of this linear numerical model and the nonlinear numerical simulations of Kindle.

a. The east-west slope of the model pycnocline

From Fig. 4, it is evident that the slope of the model pycnocline and the observed slope of the 14°C isotherm (thermocline) are similar. The slopes of the pycnocline and thermocline are steepest from 180° to 100°W , this being the region of largest mean zonal wind stress. From 180° to the western boundary, both the pycnocline and thermocline slopes are nearly flat, since the mean zonal wind stress is small or nonexistent over this area. The response of the pycnocline slope to the local winds is predictable, since the steady state balance present is given by Eq. (8). Therefore, when the imposed wind stress is small, the resulting pycnocline slope is small. From 100°W to the eastern boundary, by Eq. (8). Therefore, when the imposed wind stress is small, the resulting pycnocline slope is small. From 100°W to the eastern boundary, the pycnocline slope is again small due to the small mean wind stress

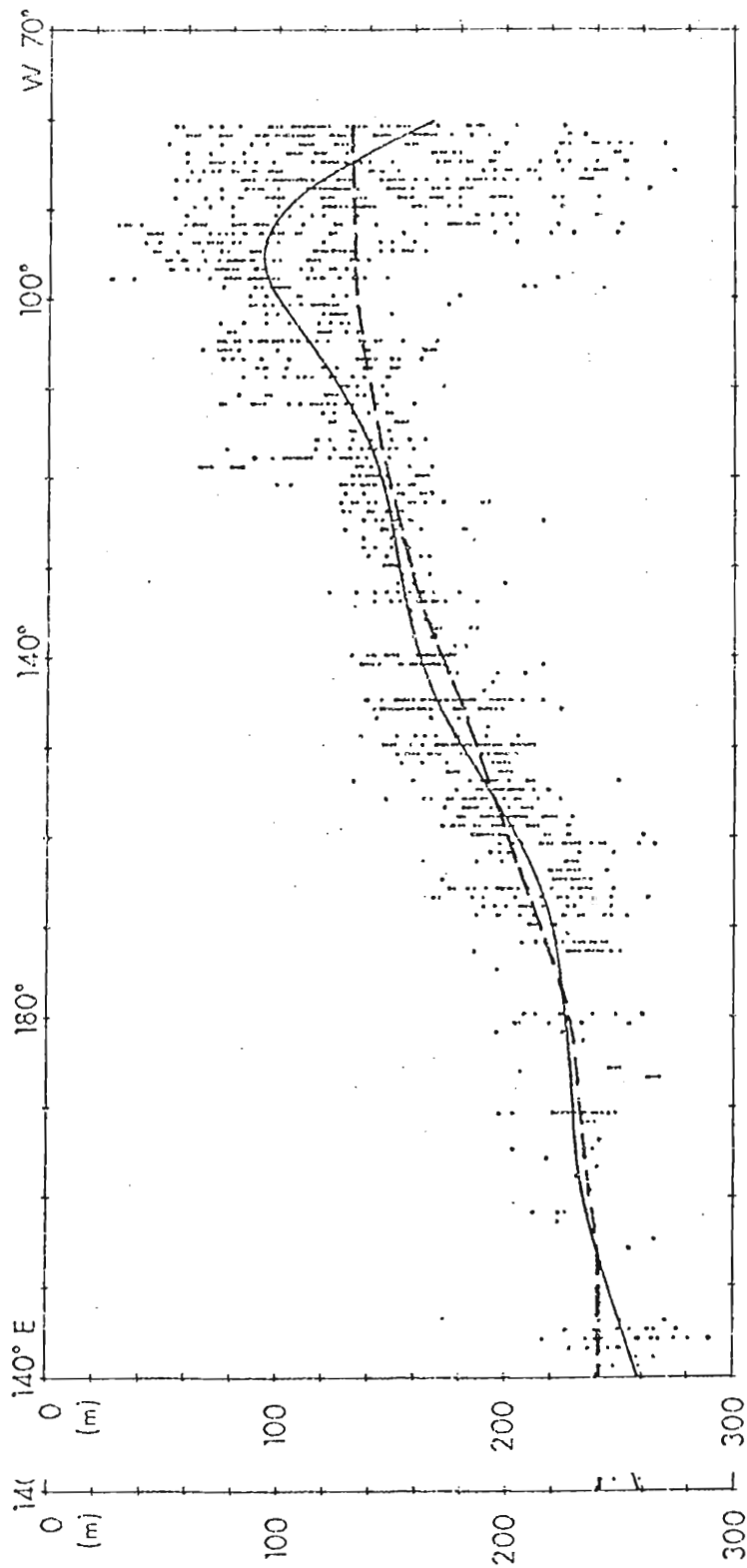


Fig. 4. Comparison of model pycnocline depth at the equator (dashed line) and mean depth of the 14°C isotherm (solid line) for a scatter diagram of observations between 10°N and 10°S (scatter diagram from Meyers, 1979b).

present. The high degree of scatter present near the eastern boundary is indicative of El Niño and other inter-annual events present in the data set (Meyers, 1979b).

The important features of Fig. 4 are that the model pycnocline is depressed by 40 meters in the west and is welled upward by 70 meters in the east. For the entire width of the basin, the position of the model pycnocline always falls within a 60 meter thick envelope provided by the observations. The two curves differ by less than 20 meters in the central and western Pacific.

The greatest discrepancy between the model results and the observations occurs within the longitudinal band from 80°W to 100°W. Besides the obvious depth difference, there is a difference in the character of the slopes. The slope of the model pycnocline is flat, whereas, the thermocline decreases in depth offshore and then increases in depth near 95°W. The expression of the wind stress forcing in this band may account for these differences.

Averaging the zonal wind stress across the 80°W-100°W band yields a near zero mean of $-.002 \text{ N m}^{-2}$, but inspection of Fig. 5 shows that the wind stress within this band may range from $-.02 \text{ N m}^{-2}$ at 100°W to $.02 \text{ N m}^{-2}$ at 80°W. The mean stress across this band is still small, but the spatial variance is large. This may account in part for the difference in slopes at the eastern boundary. If this band was resolved better, then upwelling favorable winds (negative) near 100°W would decrease the depth of the model pycnocline and downwelling favorable winds (positive) would depress the pycnocline near the boundary. This type of wind the depth of the model pycnocline and downwelling favorable winds (positive) would depress the pycnocline near the boundary. This type of wind stress forcing would create a pycnocline depth minimum similar to that

MEAN ANNUAL ZONAL WIND STRESS

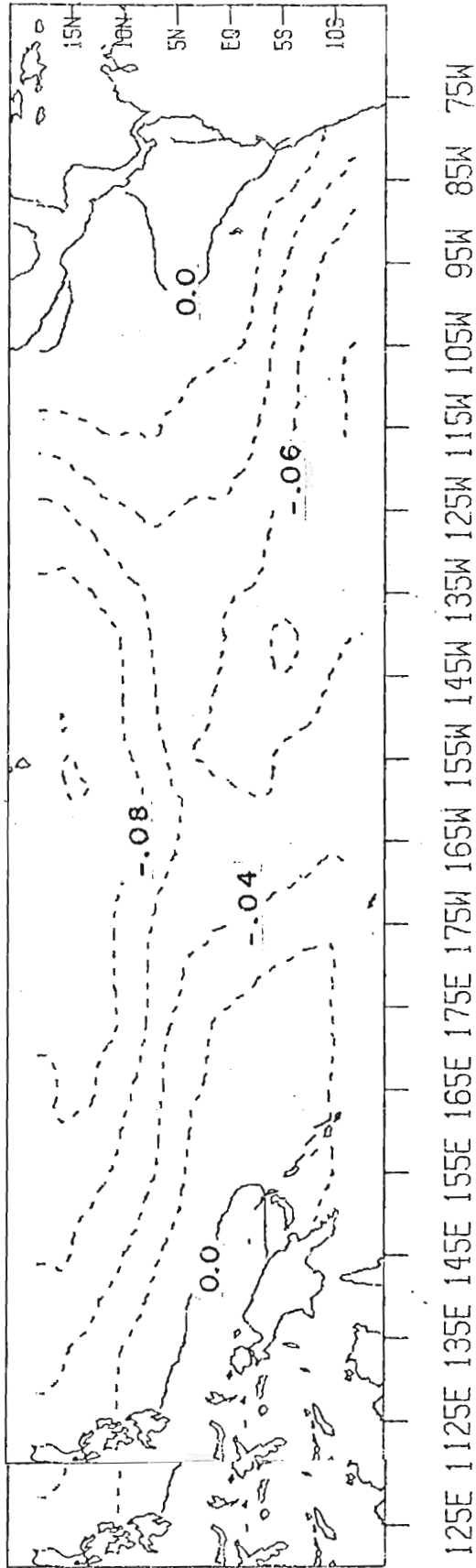


Fig. 5. Mean annual zonal wind stress across the model basin for the MASIG wind stress data for 1961-1970. Dashed contours indicate an easterly wind stress. Contour interval is $.02 \text{ Nm}^{-2}$.

in the observations. However, it is doubtful that even the magnitude of the wind stresses in Fig. 5 could account for the total difference between the observations and the model results. The wind stress used in the model as a forcing function was derived from surface wind observations using a constant drag coefficient for the entire data base. If this constant drag coefficient is an underestimate for the eastern boundary region, as some think it may be, then the magnitude of the wind stress would be underestimated (Meyers, personal communication). The inclusion of a non-constant c^2 in the momentum equation, would also change the pycnocline depth.

b. The seasonal response in the eastern equatorial Pacific

To interpret the model results, contour plots of the equatorial U field and H field over a period of one year prove to be very useful. Changes in the PHA at the equatorial eastern boundary during a one year period are also of interest. Fig. 6a clearly reveals a definite semi-annual signal present in the eastern tropical Pacific zonal flow field. As expected, a large part of the upper layer flow throughout the year (January-March, June-September) is directed westward, since the overlying wind field is predominantly westward. During April-June and October-December, the westward surface flow is weakened and actually reverses. This semiannual response is of interest, since the zonal wind stress exhibits strong second harmonics only in the region from 120°W to 180° (Fig. 3). During those times of the year when an eastward surface flow is present at the eastern boundary, the superposition of Kelvin waves and Rossby waves must be such that a strong eastward component is generated.

A semiannual signal is also represented in the eastern equatorial H field response (Fig. 6b). The remainder of the basin reflects the balance between the pressure gradient and the zonal wind stress. Now narrowing in on the semiannual response at the eastern boundary, Fig. 7 is a comparison between observations of the thermocline displacement (Meyers, 1979b) and the predicted equatorial PHA at the eastern boundary. Qualitatively, the same basic features are present in both curves. There is a shoaling of the pycnocline during the late winter-early spring and during the late summer-early fall and a deepening of the pycnocline during the late spring-early summer and during the late fall-early winter. In terms of phase the linear model results tend to lead the observations by 1-2 months. The amplitude of the PHA at the eastern boundary is also underestimated by the model. Though there is some difference in phase and amplitude, the results are not disheartening, rather we see that the simple linear model does in fact succeed in producing a second harmonic response remote from any region with a semiannual wind stress signal. As was stated earlier, the zonal wind stress exhibits strong second harmonics only in the region 180° to 120° W.

The generation of the eastern boundary response is reflected in the height field changes over the eastern half of the basin during the last nine months of year 4. Since the wind stress forcing is periodic, Kelvin waves are continually being generated in the interior. For the sake of simplicity, one can think of each cycle of the wind stress as generating a double Kelvin wave consisting of a downwelling leading edge and an upwelling trailing edge. generating a double Kelvin wave consisting of a downwelling leading edge and an upwelling trailing edge.

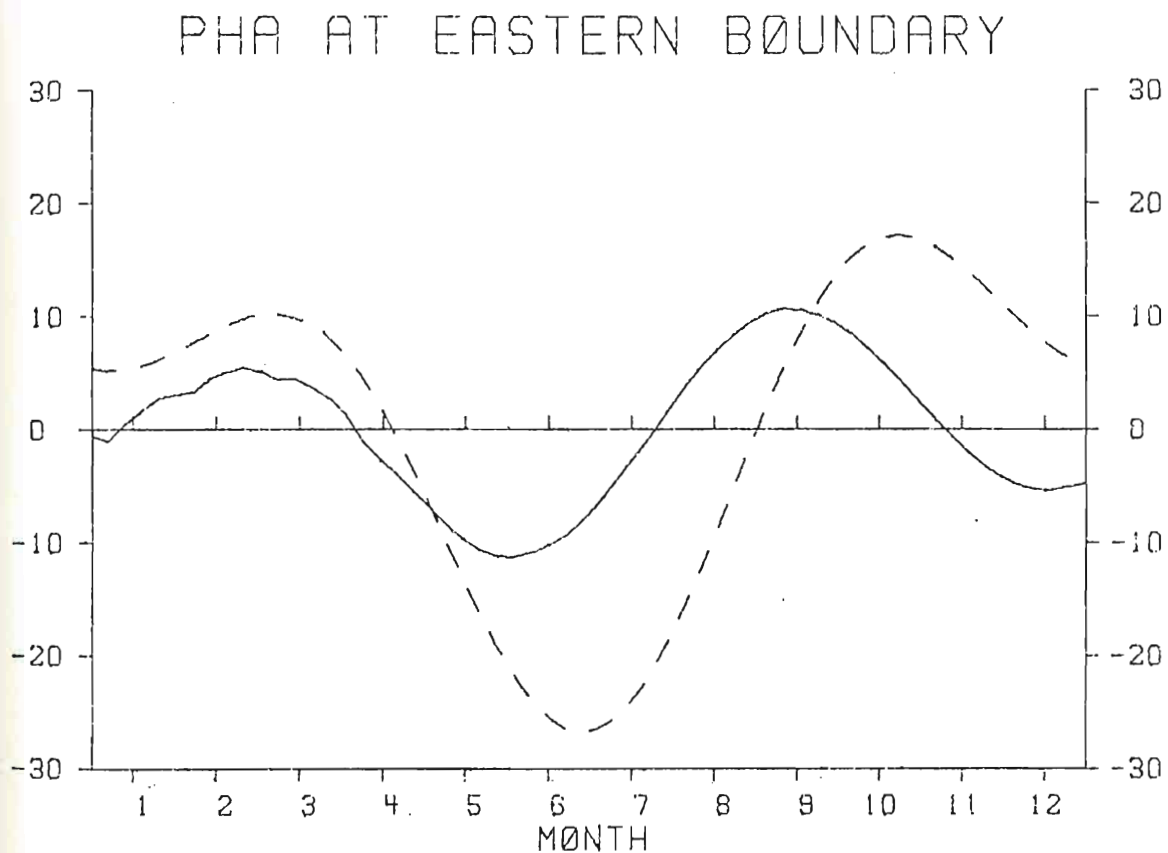


Fig. 7. Comparison of the pycnocline height anomaly (PHA) at the eastern boundary (solid line) and the seasonal variation about the mean depth of the 14°C isotherm within the band 80°W to 100°W at the equator (dashed line from Meyers, 1979b). Depth variations in meters.

The large amplitude response at the eastern boundary (Fig. 7) from March to September is a remote response to the large amplitude change in the interior wind stress from January to August (Fig. 3). From April to June an equatorially trapped downwelling disturbance propagates westward (Fig. 8a-c) and results in a downwelling response at the eastern boundary. This downwelling Kelvin wave front corresponds to a decrease (downwelling favorable) in the interior zonal wind stress during January-April. From April through July there is an increase (upwelling favorable) in the easterly wind stress between 120°W and 180° . The resulting height field response is an upwelling signal from July through October.

From August to October the packing of the height contours (Fig. 8e-g) along the coastline is indicative of a poleward travelling coastally trapped Kelvin wave. As the coastal radius of deformation decreases northward, the coastal Kelvin wave is trapped closer to the coastline. Moore (1968) has determined that an equatorially trapped Kelvin wave impinging on an eastern boundary results in an equatorially trapped response and a coastally trapped Kelvin wave. During November and December, first latitudinal mode Rossby waves are evident between 80°W and 100°W . This is the equatorially trapped response to the Kelvin wave impinging on the eastern boundary during the spring and summer.

The smaller cycle of the eastern boundary semiannual response begins with a downwelling disturbance propagating westward during November and December. This is a remote response to a decrease in the westward wind stress from August through October. This downwelling response is followed by a small upwelling signal (ULT not shown) corresponding to stress from August through October. This downwelling response is followed by a small upwelling signal (ULT not shown) corresponding to changes in the wind stress from November to January.

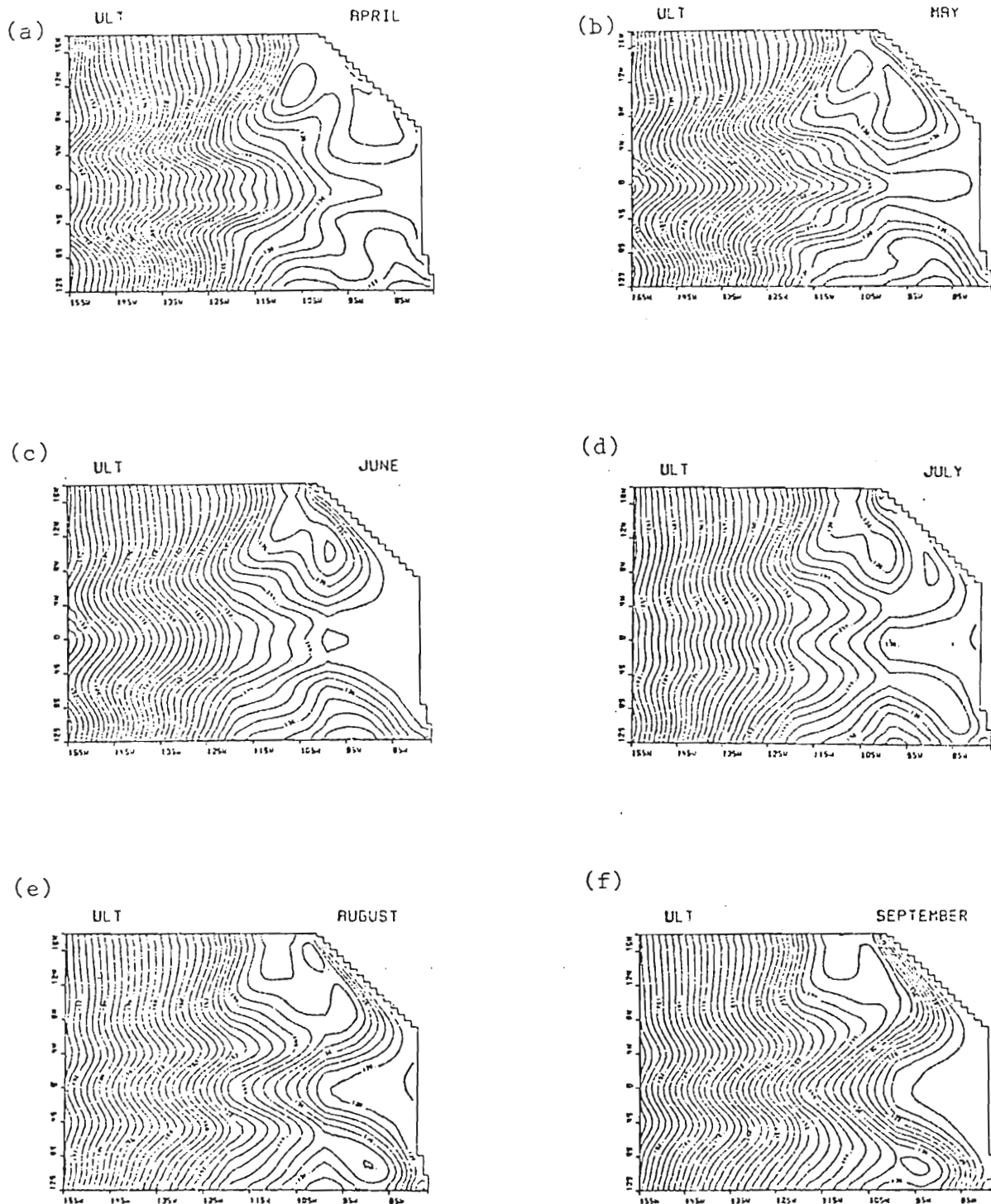


Fig. 8. Upper layer thickness over the eastern half of the model basin for the last nine months of year 4. Equatorially trapped Kelvin and Rossby waves are depicted.

Fig. 8. Upper layer thickness over the eastern half of the model basin for the last nine months of year 4. Equatorially trapped Kelvin and Rossby waves are depicted. The y-scale has been expanded to facilitate inspection of the plots. The contouring interval is 2 m.

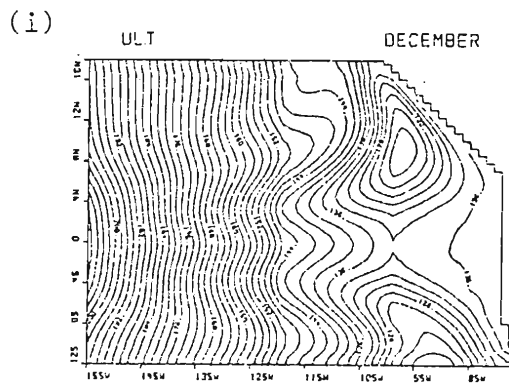
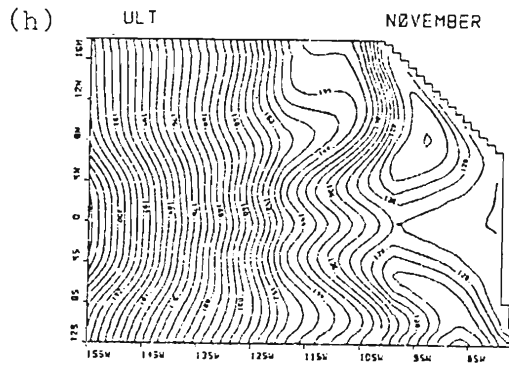
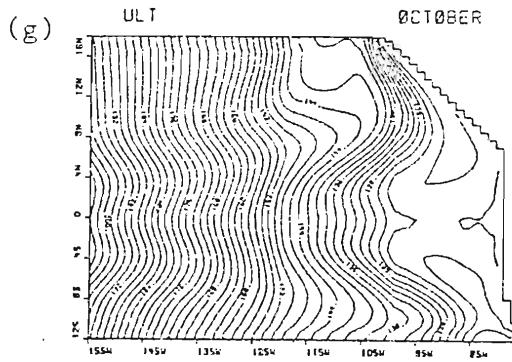


Fig. 8 (continued)

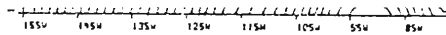


Fig. 8 (continued)

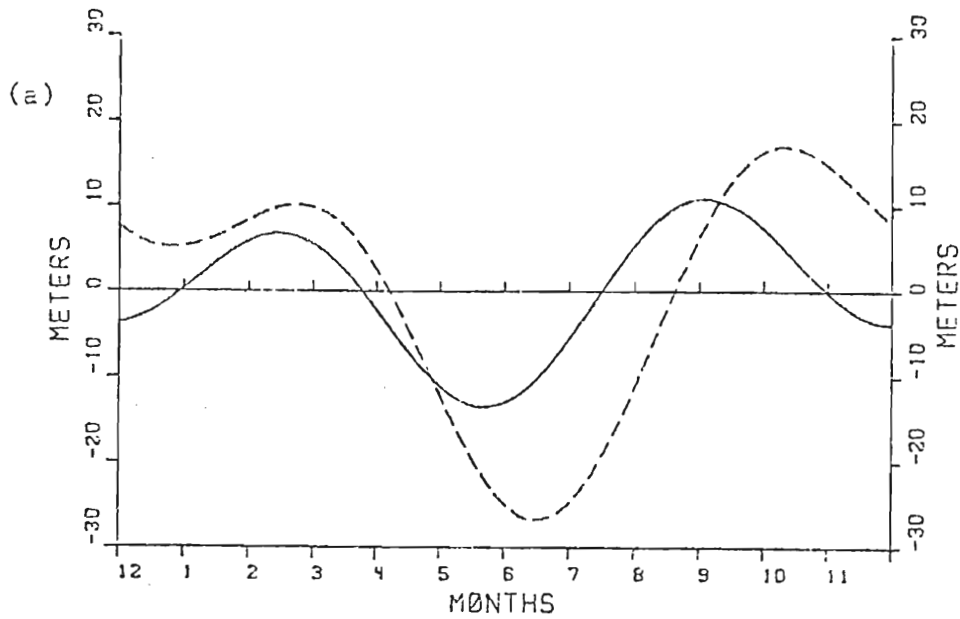
c. Comparison with a previous study.

To see how the results of this model compare with a prior investigation, the results of Kindle (1979) are used. The PHA response at the eastern boundary (Fig. 7) is a duplicate of the one presented by Kindle for his linear case (Fig. 9a). The major difference between the two linear models is that the model presented here includes an idealized coastline geometry. This, of course, may lead one to believe that the coastline geometry does not play a major role in the equatorial dynamics of the eastern Pacific. Referring back to Fig. 1, we see that the idealization of the coastline configuration at the eastern boundary about the equator (\pm radius of deformation) is merely a vertical wall. Kindle's calculations together with Fig. 8 show that the major contribution of equatorial waves to the eastern boundary response is from the incoming Kelvin waves and the associated first latitudinal mode Rossby waves reflected off the eastern boundary. The comparison of Figs. 7 and 9a tends to reinforce the findings of Kindle; i.e., if the incoming Kelvin waves and westward travelling Rossby waves are of primary importance in the eastern Pacific, then the equatorial response for the eastern boundary coastline configuration chosen here (vertical wall) should be nearly the same as the response for a linear model in a rectangular basin. Future work may require a finer resolution for the coastline approximation and a meridional boundary at the equator may not be justified at that time.

The addition of nonlinear terms to Kindle's model yields a modified eastern boundary response (Fig. 9b). Comparison of Figs. 7 and 9b shows

The addition of nonlinear terms to Kindle's model yields a modified eastern boundary response (Fig. 9b). Comparison of Figs. 7 and 9b shows that there is a slightly better phase agreement in the nonlinear

PHA AT EASTERN BOUNDARY



PHA AT EASTERN BOUNDARY

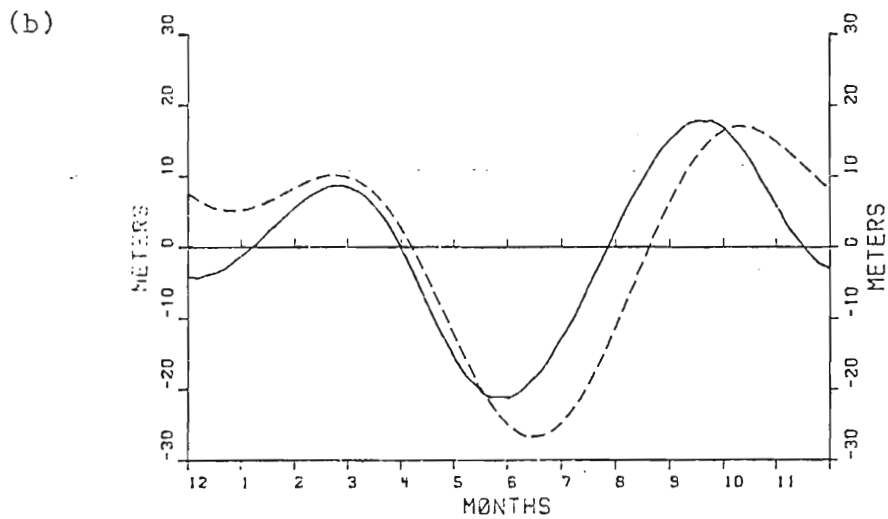


Fig. 9. Same as Fig. 7 except the solid line represents (a) the linear solution and (b) the nonlinear solution for Kindle's numerical model in a rectangular basin (from Kindle, 1979).

results, but the major contribution of nonlinear wind stress and advection terms is to increase the amplitude response.

Figures 6b and 10 show the equatorial H field during the final year of integration for the linear model presented here and the nonlinear model of Kindle. The linear model produces basically the same distribution and amplitude response as is present in the nonlinear model of Kindle. Due to the similarities present between the two model results, it is apparent that linear dynamics play a dominant role in the equatorial response.

This first model application has been used to study the oceanic response along the equator. In order to model the equatorial current system, a more descriptive set of time varying winds must be used. This type of wind stress forcing should be based on observations over the entire tropical Pacific.

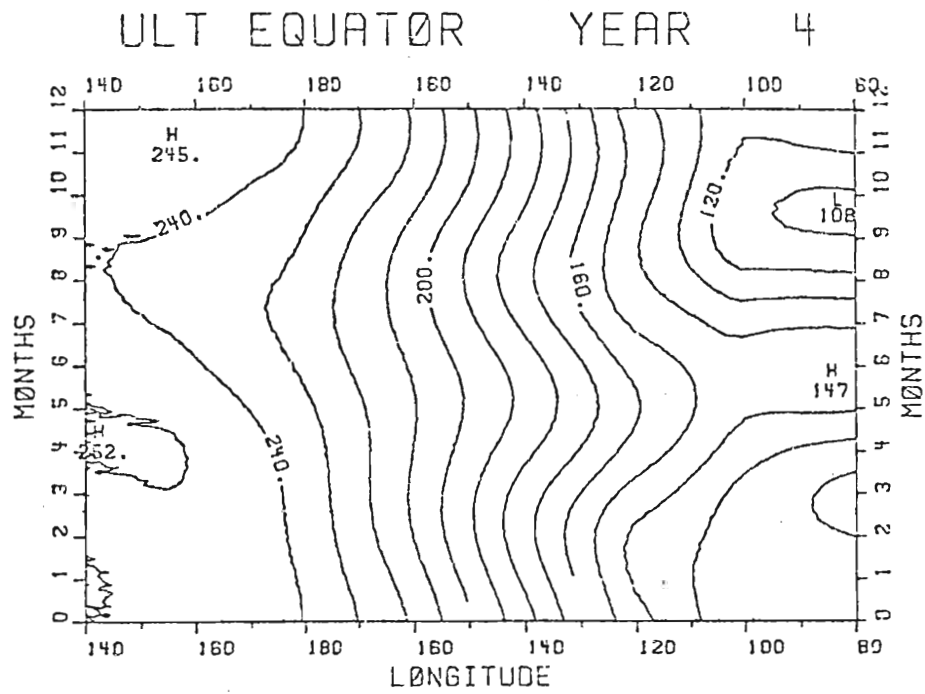


Fig. 10. Seasonal variation along the equator, of the pycnocline depth as predicted by Kindle's nonlinear numerical model (from Kindle, 1979). The contour interval is 10 m.

4. THE SEASONAL VARIABILITY IN THE EQUATORIAL CURRENT SYSTEM

The dynamic topography of the world's oceans has been used for some time now as a method to analyze the geostrophic circulation of the oceanic upper layer. The observations from numerous oceanographic expeditions were compiled by Reid (1961) in order to chart the dynamic topography over the Pacific Ocean. This dynamic topography was based on the anomaly of the geopotential distance between the sea surface and the 1000 decibar level. Reid has used the difference between the two geopotential surfaces as a means to assess the geostrophic flow field over the Pacific. The estimated geostrophic current could then be compared with existing maps and atlases of the Pacific Ocean surface flow.

With regard to the tropical Pacific, the major equatorial currents were clearly evident in Reid's map. Distinguishable geostrophic flows coincided with the westward flowing North and South Equatorial Currents separated by the eastward directed North Equatorial Countercurrent. An interesting feature indicated by the contours of geopotential anomaly was the existence of a South Equatorial Countercurrent present in the western Pacific.

Most of the observations that went into Reid's study of the dynamic topography were taken during the summer months of each hemisphere. As a result, Reid's map of geopotential anomaly represents the mean state topography here taken during the summer months of each hemisphere. As a result, Reid's map of geopotential anomaly represents the mean state

of a specific season. To gain an understanding of the time and space scales of the seasonal variability in the western Pacific Ocean, Wyrтки (1974a) has analyzed the seasonal cycle of the dynamic topography relative to 500 decibars together with the seasonal perturbations of sea level. Since the equatorial currents are stronger in the western Pacific, this was the region within which sea level and dynamic height observations were compared. The dynamic topography relative to 500 decibars was calculated using data from thousands of hydrographic stations from 30°N to 20°S and 140°E to 140°W. Sea level observations spanning the period 1951-1971 were obtained from ten islands within this same region. The analysis Wyrтки performed shows that sea level observations at island stations are an efficient and accurate method to monitor the equatorial current system.

In a subsequent paper, Wyrтки (1974b) zonally averaged the dynamic height data between 170°E and 140°W to obtain a mean meridional profile of dynamic height (Fig. 11). Observed sea level fluctuations from eight islands were then used to modulate the mean profile. This provided a time series of sea level height.

These two papers by Wyrтки provide an intriguing insight into the seasonal variability and interaction of the equatorial current system. The now familiar equatorial system of troughs and ridges is represented in Fig. 11. The difference in sea level across the major currents was used to study the seasonal response. Both the North Equatorial Current and the Countercurrent are strongest in the fall and weakest in the spring and the Countercurrent are strongest in the fall and weakest in the

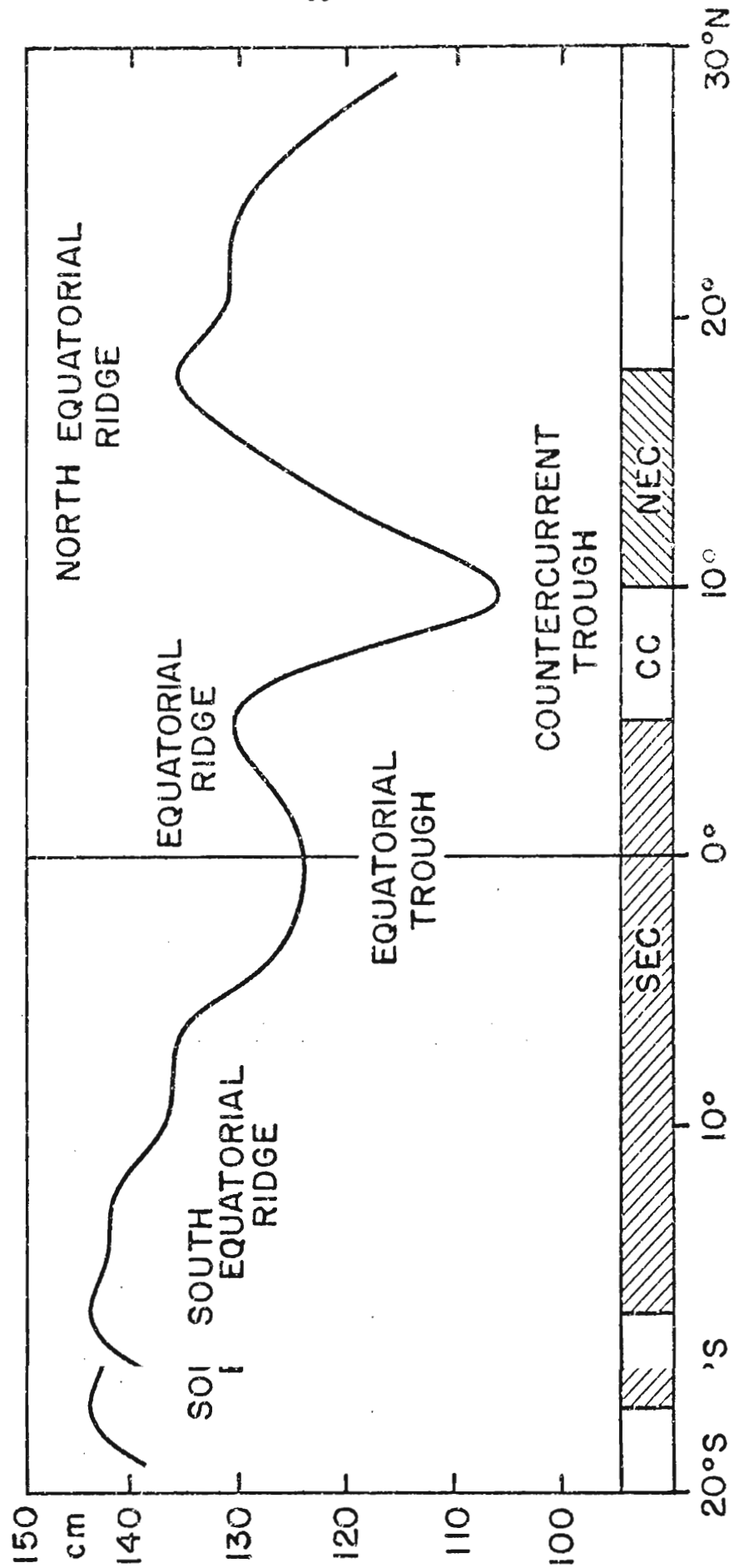


Fig. 11. Meridional profile of dynamic height relative to 500 db zonally averaged between 140°W and 0°W and 170°E (from Wyrtki, 1974b).

spring (Fig. 12). The South Equatorial Current is generated by contributions from the sea level difference between the South Equatorial Ridge and the Equatorial Trough and the height difference between the Equatorial Ridge and the Equatorial Trough. The seasonal cycle of the South Equatorial Current is out of phase with the two Northern Hemispheric currents, i.e., stronger in the spring and weaker in the fall. Wyrтки denotes that the observations of the Equatorial Undercurrent by Taft and Jones (1973) indicate that the South Equatorial Current and the Undercurrent are in phase.

The seasonal variability of sea level difference across the equatorial currents is, of course, the combined response of the fluctuations in sea level heights of the troughs and ridges. For example, Wyrтки's sea level data indicate that the North Equatorial Ridge decreases in height from March to June and increases in height from August to November. The Countercurrent Trough experiences an increase in sea level from March to June and decreases in sea level from November to January. This results in the North Equatorial Current being weak in the spring and strong in the fall.

In this section a numerical simulation is performed in which the model is driven by mean monthly wind stresses based on actual observations over the tropical Pacific. The wind stress data was derived from the compilation of wind stress observations of Wyrтки and Meyers (1975a, b). Their work consisted of averaging each subset of observations from a total of five million Pacific Ocean surface observations within 2° latitude by 10° longitude quadrangles covering the Pacific from 30°N a total of five million Pacific Ocean surface observations within 2° latitude by 10° longitude quadrangles covering the Pacific from 30°N

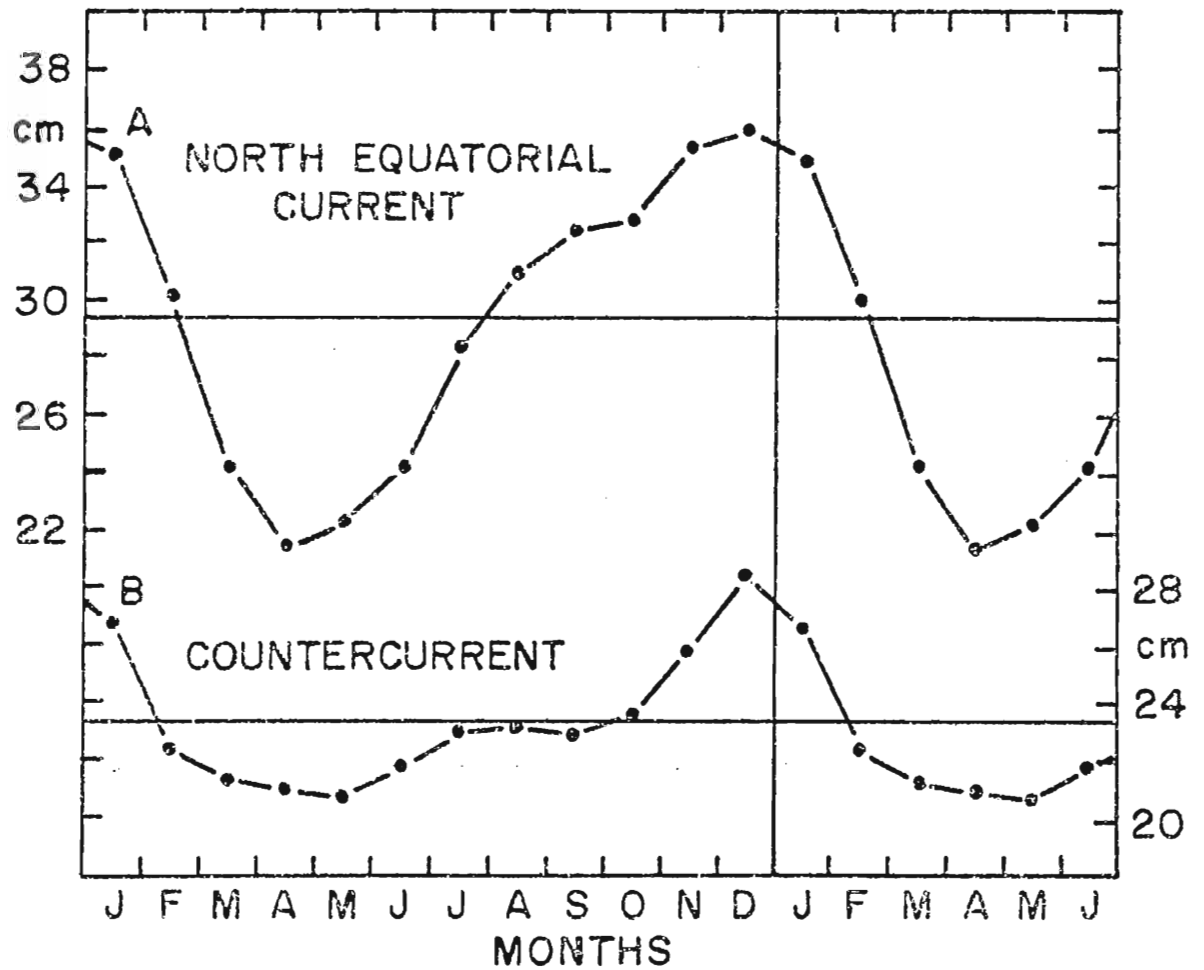


Fig. 12. Mean annual variation of sea level difference across the North Equatorial Current (A) and the Countercurrent (B) (from Wyrtki, 1974b).

North Equatorial Current (A) and the Countercurrent (B) (from Wyrtki, 1974b).

to 30°S for each month from 1947-1972. Each wind observation was converted to wind stress using the formula $\vec{\tau} = \rho_a C_D |\vec{W}| \vec{W}$, where $\vec{\tau}$ is the wind stress, ρ_a is the air density, C_D is the drag coefficient and \vec{W} is the wind velocity. The air density was assumed to be constant at 1.2 kg/m³ and a constant drag coefficient of 1.5×10^{-3} was chosen. Though the work of Wyrтки and Meyers was an exhaustive study, there still remained regions of the Pacific with a paucity of observations. If this data base is to be used to drive a numerical model, the "holes" in the data set would have to be eliminated.

During 1978, the Mesoscale Air-Sea Interaction Group at Florida State University developed a ten year (120 month) wind stress data set in which the wind stress was evaluated monthly at each point on a 2° by 2° grid for the Pacific Ocean from 30°N to 30°S. This was accomplished by analyzing subjectively Wyrтки and Meyers' wind stress data for the years 1961-1970; these being the years with a consistently large number of observations and also encompassing an El Niño event. For the present study at hand, the MASIG data set was averaged over the full ten years to obtain a long term mean monthly wind stress value at every point on the 2° by 2° mesh for each of the 12 months. Hopefully, what resulted is a data set representative of the mean monthly features in the Pacific wind stress field based on ten years of observations. It is the portion from this mean monthly wind stress data for 18°N to 12°S that is used to drive the model over a period of four years. This model application was designed to determine whether or not the resulting response is indicative of the Pacific Ocean equatorial current system. All the model designed to determine whether or not the resulting response is indicative of the Pacific Ocean equatorial current system. All the model results that follow are from year four of the integration.

Since the model results will be compared with Wyrтки's dynamic topography and sea level studies between 170°E and 140°W, the first discussion of the model results will be restricted mainly to this region. The major topographic features of the equatorial current system are clearly reflected in the meridional profile of the model pycnocline (Fig. 13). All terminology describing the topographic features of the model pycnocline will be consistent with those used to describe the sea surface topography. The features present are the pycnocline representation of the North Equatorial Ridge at 17°N, the Countercurrent Trough at 8°N, the Equatorial Ridge at the equator, the Equatorial Trough at 2°S and the South Equatorial Ridge at 10°S. When this pycnocline profile is compared with Wyrтки's sea level profile (Fig. 11), it is strikingly apparent that this simple linear model forced by real wind stresses is capable of producing a response very similar to that of the equatorial current system. The meridional slope of the model pycnocline north of the equator is also in agreement with observations of the meridional slope of the thermocline beneath the Countercurrent and the North Equatorial Current (Knauss, 1962). It should be pointed out that the variations in depth of the pycnocline are roughly 180° out of phase with the observed deviations in sea level. This is further justification that the reduced-gravity approach taken in this problem is valid.

Having presented the similarity between the meridional slope of the pycnocline and observations, the differences between the profiles of the pycnocline and observations, the differences between the profiles

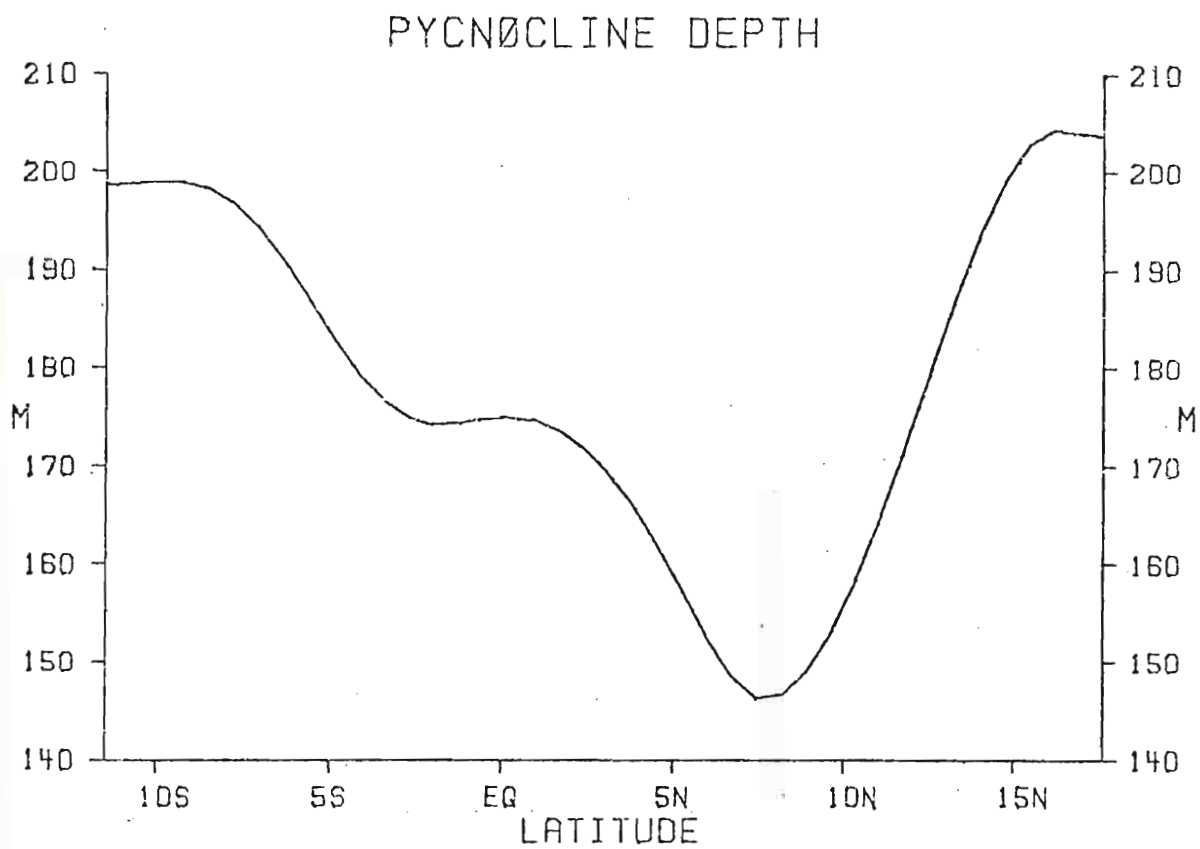


Fig. 13. Meridional profile of model pycnocline depth zonally averaged between 140°W and 170°E.

must now be addressed. One of these differences is that the location of the troughs and ridges in the pycnocline profile appears to be shifted 2° southward from the trough-ridge system in the sea level profile. Another difference between the two profiles becomes evident when the pycnocline depth variations are transformed into dynamic centimeters. The pycnocline depth difference between adjacent troughs and ridges is one-third to one-half the difference exhibited in the sea level profile.

There may be several reasons for the discrepancies in location and depth across the troughs and ridges. First of all, this is only a linear model so the addition of nonlinearities, especially from a non-constant c^2 term could result in a more drastic topography of troughs and ridges. Secondly, the mean monthly wind stress forcing used in this model was based on 10 years of observations, whereas the meridional profile of sea level was based on 21 years of observations. There is a possibility that this pycnocline profile is indicative of a small deviation in time from the long term average sea level profile. A firm explanation cannot be provided until the spatial distribution of the curl of the MASIG wind stress data is determined. Finally, due to the simplicity of the model, only the gravest baroclinic mode can be accounted for, thus higher order modes are neglected. These higher order modes would definitely modify the present solution. It would be interesting to know how nonlinearities and a greater degree of vertical resolution would affect the pycnocline profile.

It would be interesting to know how nonlinearities and a greater degree of vertical resolution would affect the pycnocline profile.

The seasonal cycles of the pycnocline slope and zonal velocities of the equatorial currents are depicted in Figs. 14-19. The latitudinal location of the various currents was taken to be marked by the mean monthly position of the appropriate trough and ridge. The seasonal signal for the North Equatorial Current (Figs. 14, 15) is not periodic due to the presence of a subtropical mode Rossby wave at the northern boundary. This Rossby wave is one remaining transient in the solution. It was generated during spin-up and is slowly propagating out of this region of interest. Smoothing along the open boundary has a small dissipative effect on the depth of the North Equatorial Ridge. The major feature discernible in these plots is that the velocity and slope across the North Equatorial Current are maximum in the summer months. A definite annual response is present in the Countercurrent signals (Figs. 16, 17). Minima in pycnocline slope and zonal velocity occur during the winter-spring period and maxima occur during summer and fall. The pycnocline slope and zonal velocity associated with the South Equatorial Current also display an annual signal (Figs. 18, 19). The slope and velocity are maximum during the winter and spring and have minimum values in the summer and fall.

The variation in pycnocline depth (Fig. 16) across the Countercurrent may be compared with the mean annual variation of sea level difference across this current (Fig. 12). The model results show that the pycnocline slope across the Countercurrent begins to increase in April and decreases sharply in November. The observed slope in sea level across the Countercurrent begins to increase in May, remains constant and decreases sharply in November. The observed slope in sea level across the Countercurrent begins to increase in May, remains constant from July to October, increases from October to December and then

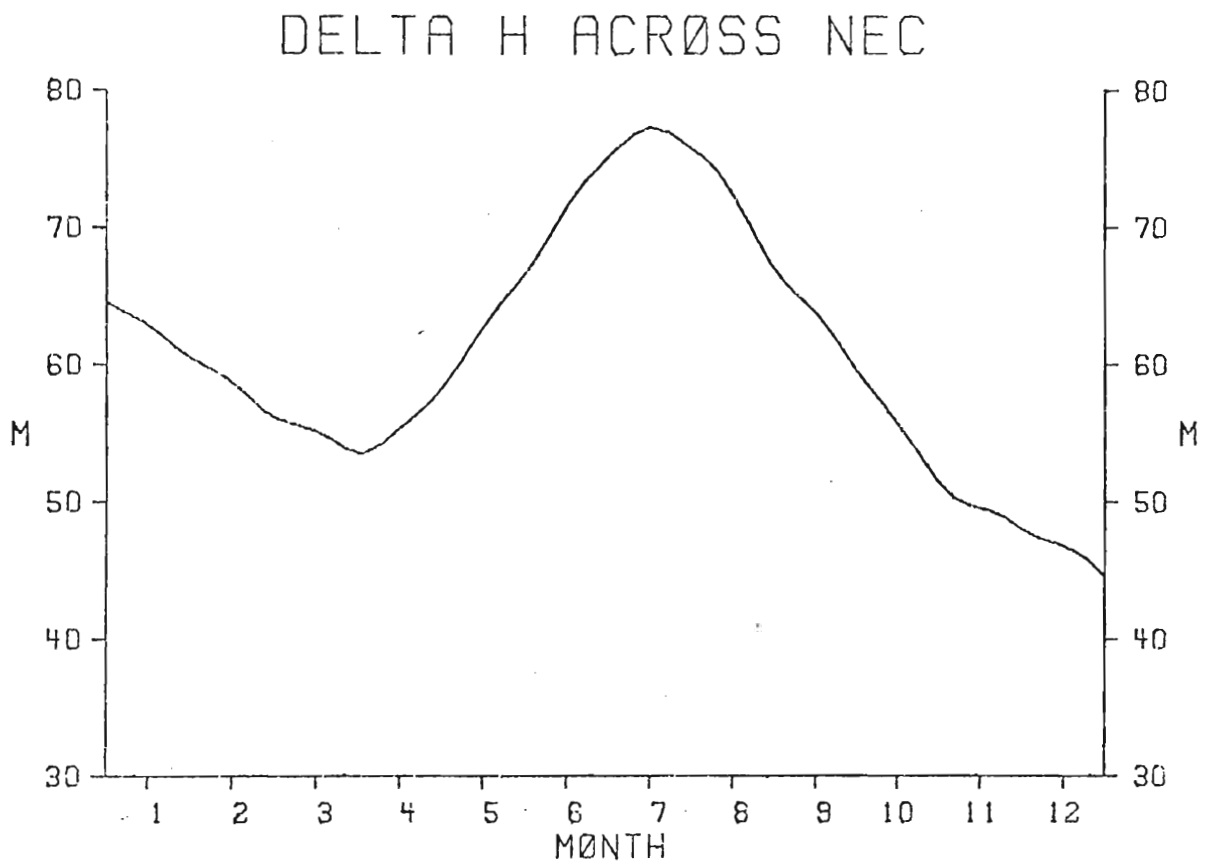


Fig. 14. Pycnocline depth difference across the North Equatorial Current.

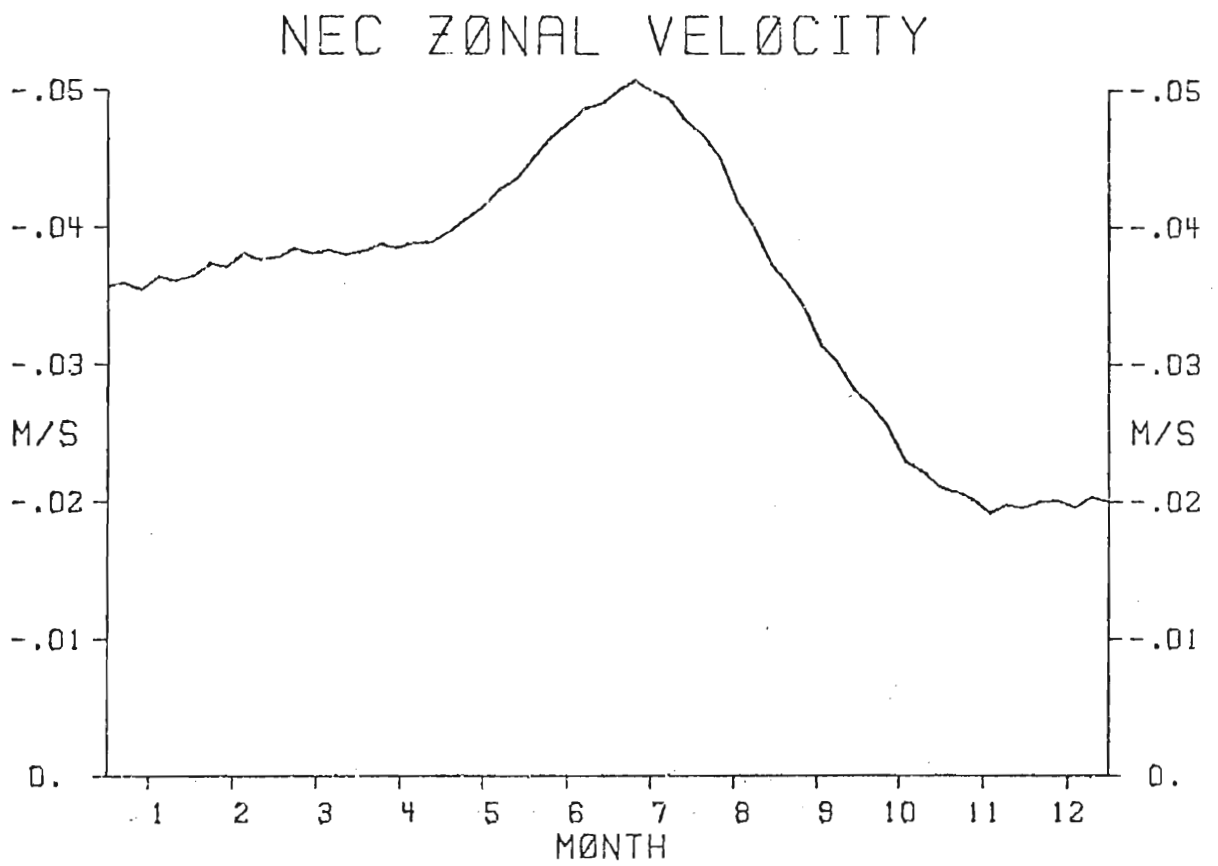


Fig. 15. North Equatorial Current zonal velocity averaged between 140°W and 170°E.

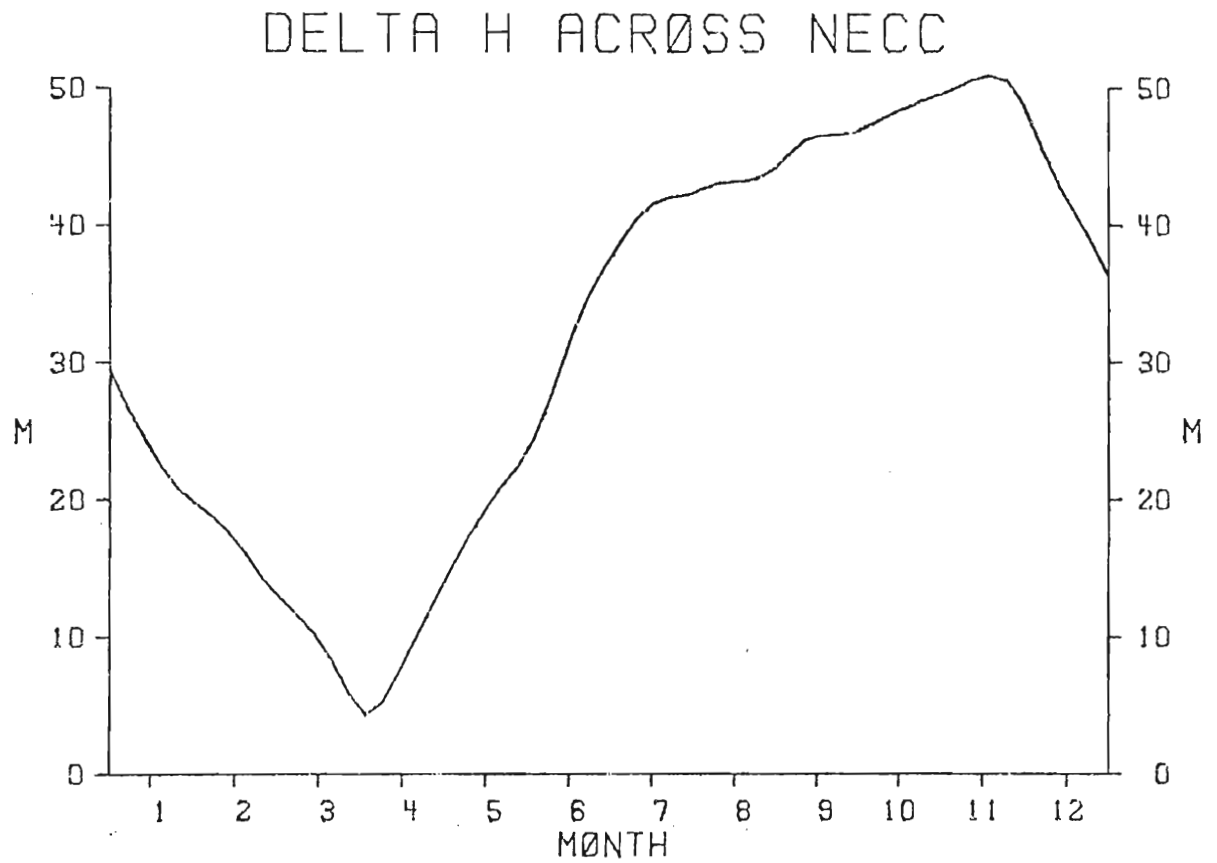


Fig. 16. Pycnocline depth difference across the North Equatorial Countercurrent.

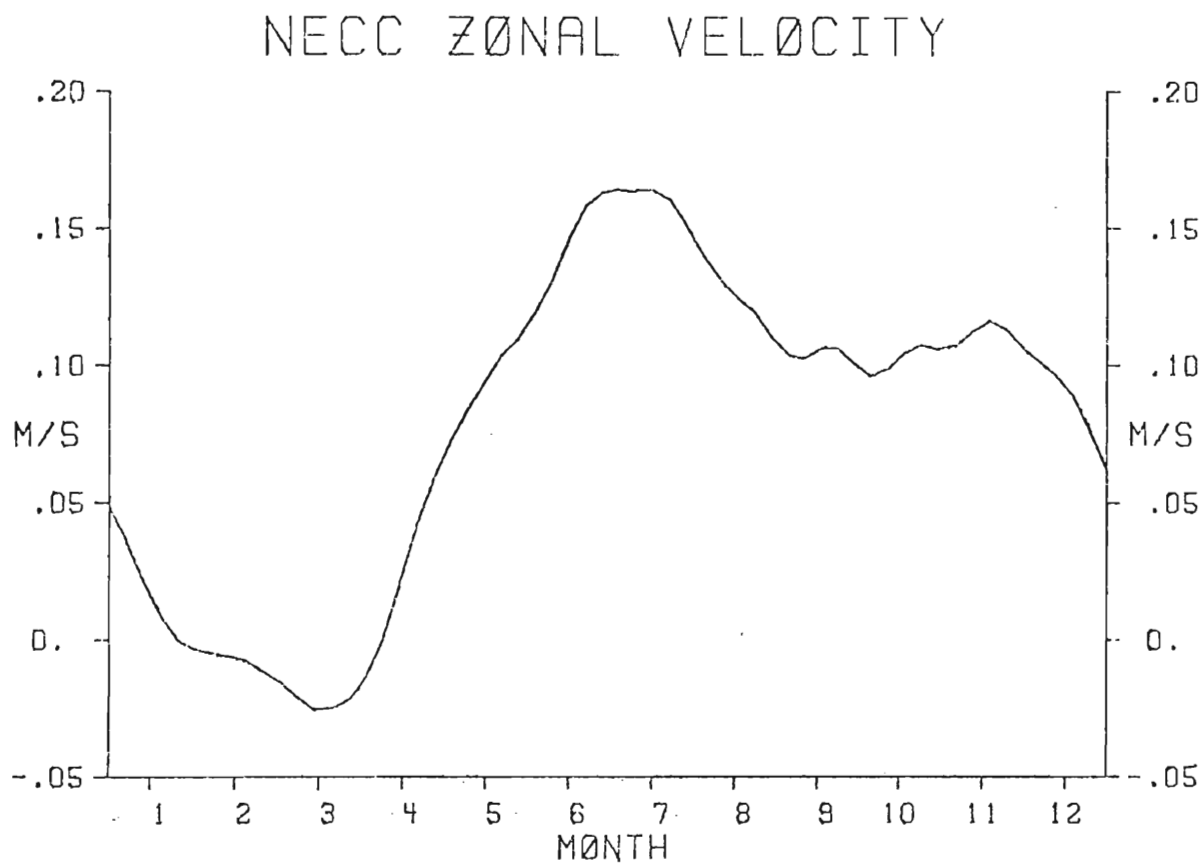


Fig. 17. North Equatorial Countercurrent zonal velocity averaged between 140°W and 170°E.

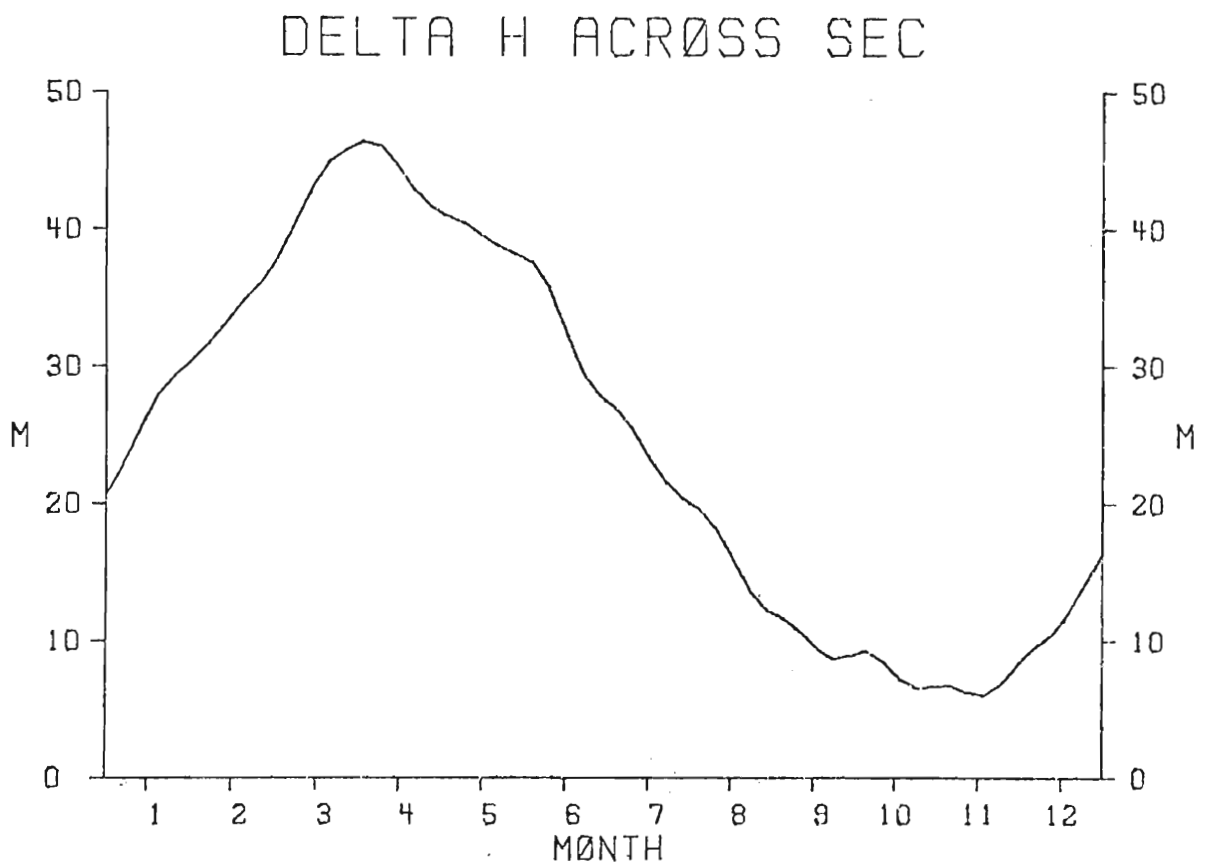


Fig. 18. Pycnocline depth difference across the South Equatorial Current.

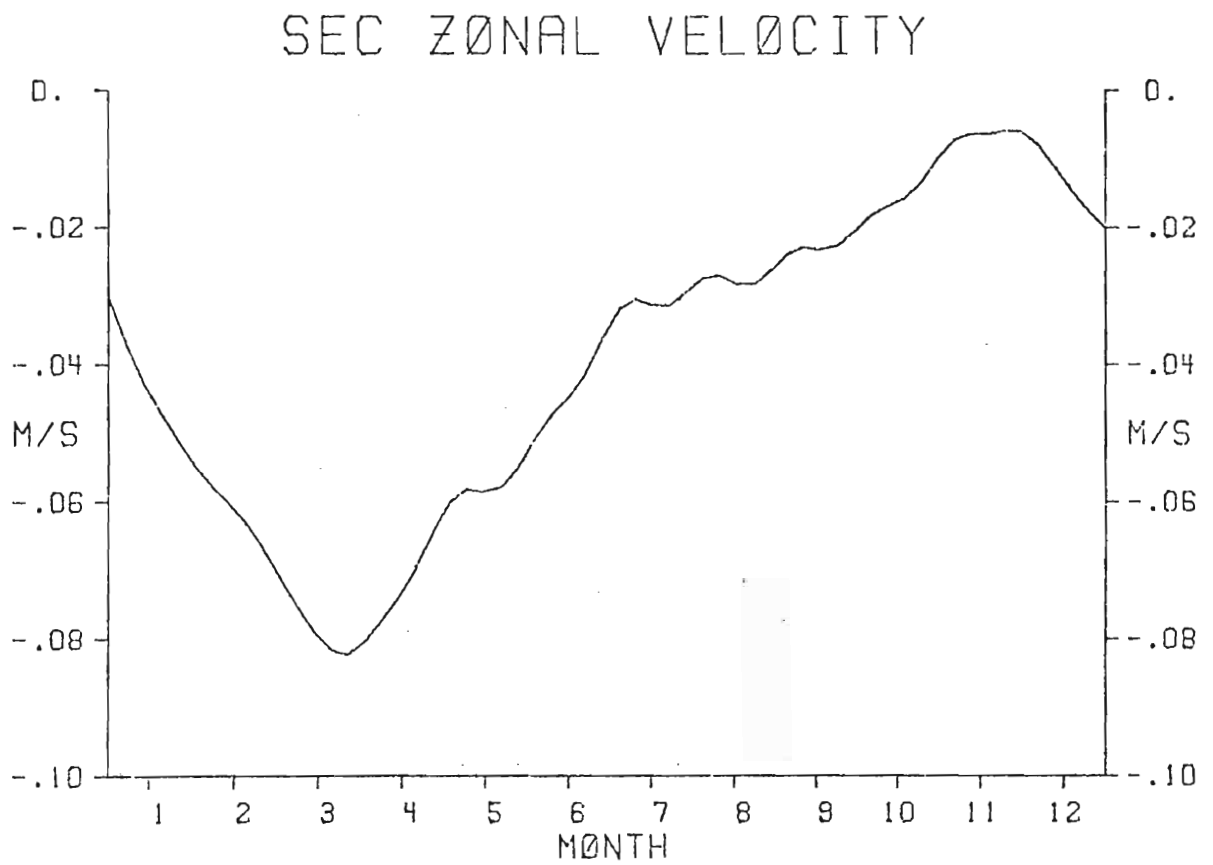
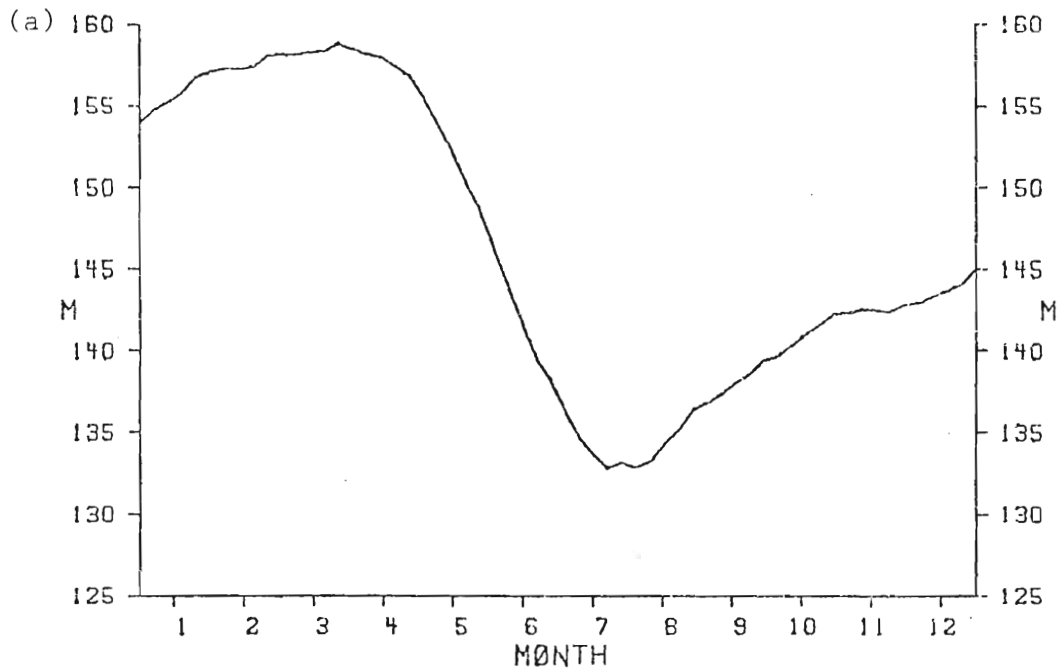


Fig. 19. South Equatorial Current zonal velocity averaged between 140°W and 170°E.

decreases. The pycnocline slope across the Countercurrent is the combined result due to the depth of the Countercurrent Trough and the depth of the Equatorial Ridge (Fig. 20). The pycnocline depth beneath the Countercurrent Trough is deepest from January to June and is shallow from June to December. This corresponds to Wyrтки's (1974a) assessment that the Countercurrent Trough is highest from March to June and lowest from November to January. According to Wyrтки, high sea level occurs near the equator from November to January. The model results indicate that the maximum depth of the pycnocline beneath the Equatorial Ridge occurs from September to January. From these various comparisons it may be concluded that the linear model results for the Countercurrent tend to lead the observations by approximately two to three months.

The best agreement with observations is produced by the model representation of the South Equatorial Current. Wyrтки (1974a) has shown that the sea level difference from Pago Pago (14°S) to Canton (3°S) is a maximum in June and a minimum in December (Fig. 21). The model pycnocline slope displays a maximum in April and a minimum in November. Using observations of surface current speeds, Wyrтки has shown that between Canton and Samoa (14°S) the strongest flow occurs in March and the weakest flow occurs in November. This is precisely what is depicted in Fig. 19. Since the variation in depth between the South Equatorial Ridge and the Equatorial Trough (Fig. 18) is in phase with the seasonal variation of the South Equatorial Current (Fig. 19), it is obvious that this current is geostrophically forced. Based on observational evidence, Wyrтки has shown that the seasonal variation of it is obvious that this current is geostrophically forced. Based on observational evidence, Wyrтки has shown that the seasonal variation of the South Equatorial Current and the Countercurrent are opposite in

NECC TROUGH DEPTH



EQUATORIAL RIDGE DEPTH

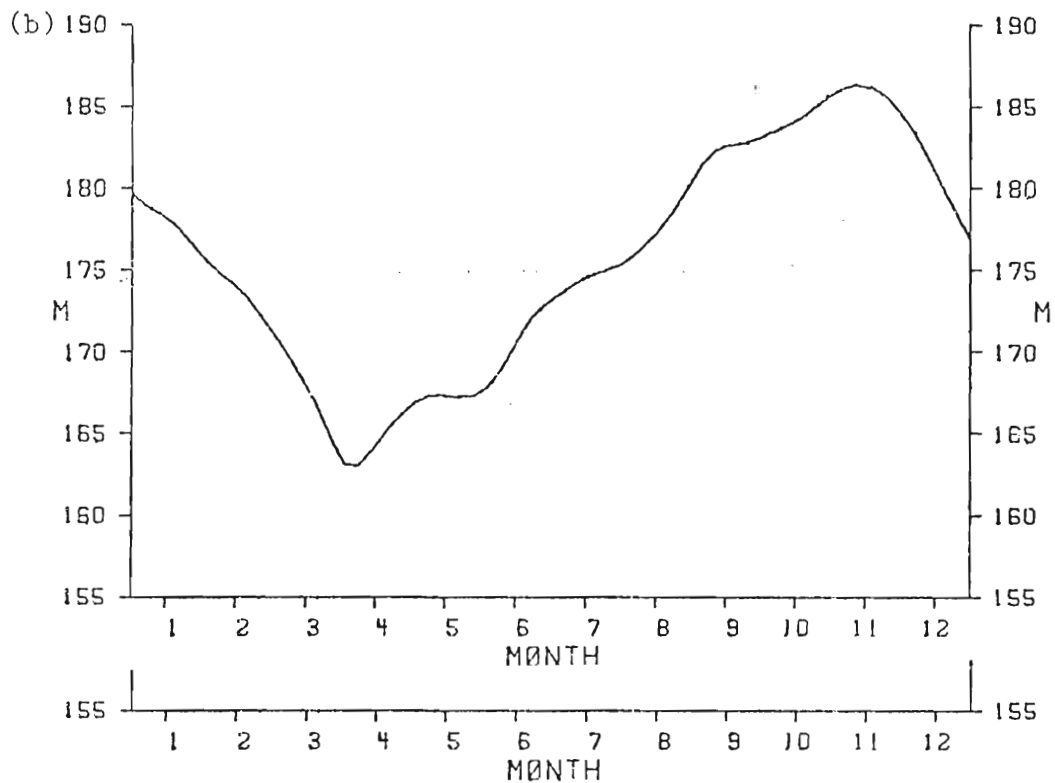


Fig. 20. Pycnocline depth beneath (a) the Countercurrent Trough and (b) Equatorial Ridge.

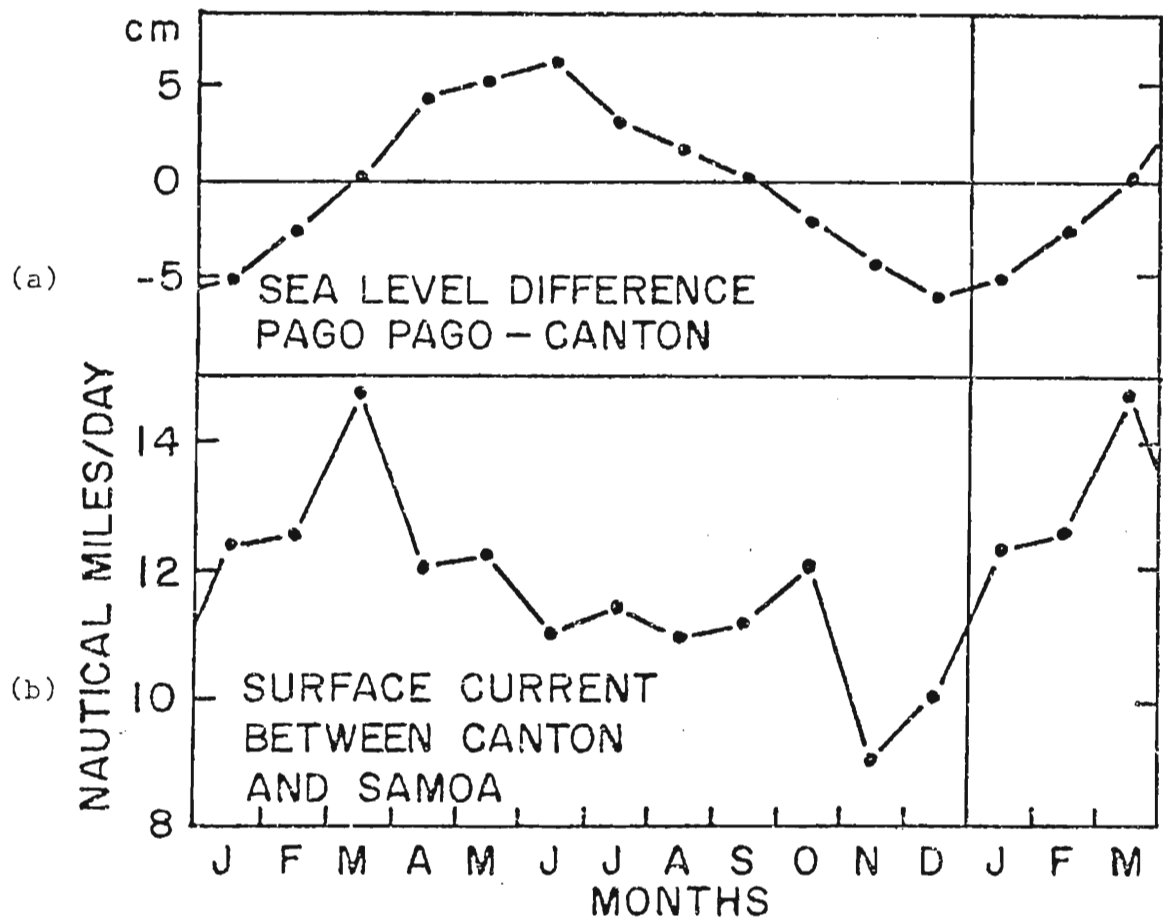


Fig. 21. Seasonal variation of (a) sea level difference between Pago Pago and Canton and (b) surface current between Canton and Samoa (from Wyrcki, 1974a).

Pago Pago and Canton and (b) surface current between Canton and Samoa (from Wyrcki, 1974a).

phase. A comparison of Figs. 17 and 19 shows that this also holds true for the model results.

As demonstrated in several models (Yoshida, 1955; Federov, 1961; Meyers, 1975), the vertical displacement of the pycnocline is governed by the curl of the wind stress. A positive curl implies upwelling and a negative curl results in downwelling. Wyrтки and Meyers (1975a) have computed and mapped the curl of the bimonthly and annual mean wind stress for their 25 years of data. For the purpose of comparison, it will be assumed that the spatial distribution of the wind stress curl from Wyrтки's and Meyers' data is representative of that for the 10 year MASIG data set.

For the area 170°E - 140°W and 18°N - 12°S , Wyrтки and Meyers' map of the curl of the annual mean wind stress displays three distinct regions. From 18°N - 14°N there is a region of negative wind stress curl. The downwelling produced by this curl results in the pycnocline depth maximum beneath the North Equatorial Ridge (Fig. 13). Centered at 8°N is a region of positive wind stress curl. The upwelling generated within this area of wind stress curl is manifested by the pycnocline depth minimum beneath the Countercurrent Trough. Another region of negative wind stress curl is centered at 12°S . The Ekman pumping associated with this region of negative curl produces a pycnocline depth maximum beneath the South Equatorial Ridge.

Bimonthly maps of the wind stress curl for November-February depict a region of positive wind stress curl at 3°S - 5°S . This seasonal variability deepens the equatorial trough and thus increases the westward geostrophic flow. This response is the seasonal strengthening of the South Equatorial Current (Figs. 18, 19).

The simple dynamics present in this model permit a response in which the wind stress curl sets up a system of troughs and ridges. The difference in depth across these troughs and ridges produces a meridional pressure gradient. The pressure gradient in turn, geostrophically forces zonal currents.

Outside the region from 170°E to 140°W there are other aspects of the model results deserving of attention. In the eastern half of the basin (Fig. 22) the Countercurrent Trough has a noticeable northward shift from 155°W to 115°W . Wyrтки (1974a) has reported that the mean annual dynamic topography between 170°E and 140°W displays a meridional displacement from 8°N to 10°N . Across this same latitudinal band the upper layer thickness (Fig. 23) shows a northward shift in the Countercurrent Trough from 7°N to 11°N . The location of the Countercurrent Trough across the basin is reminiscent of the path taken by a third latitudinal mode Rossby wave observed during a preliminary trial of this model designed to generate free equatorial waves (O'Brien, et al., 1980). Further inspection of Fig. 22 reveals the existence of a southwestward propagating upwelling disturbance near 8°N . The velocity and location of this annual feature resemble that of a third latitudinal mode Rossby wave. The westward movement of this upwelling perturbation has a definite effect on the seasonal signal of the Countercurrent Trough. The presence of this disturbance contributes to the formation of a pycnocline depth minimum beneath the Countercurrent Trough during July and August (Fig. 20a).

A similar phenomenon has been studied in two separate works concerning August (Fig. 20a).

A similar phenomenon has been studied in two separate works concerning an annual Rossby wave in the tropical North Pacific. Both White

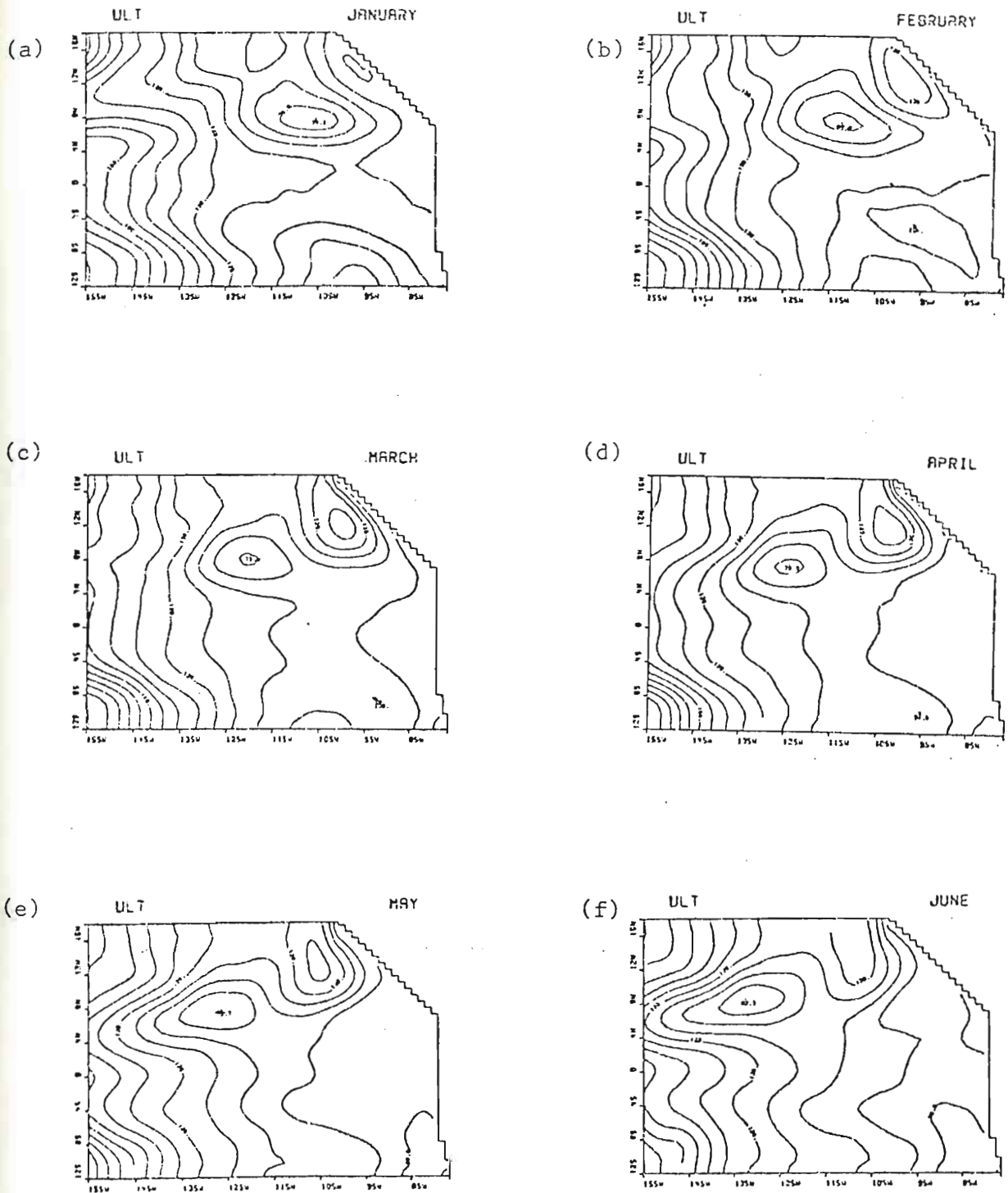


Fig. 22. Upper layer thickness over the eastern half of the model basin during year 4. The y-scale has been expanded to facilitate

inspection of the plots. The contouring interval is 10 m.

(1977) and Meyers (1979a) use Eq. (5) to study the combined response of local Ekman pumping and nondispersive Rossby waves. White confines his attention to the region 10°N - 20°N . He has ascertained that the interior response to local forcing is modulated by baroclinic Rossby waves. Meyers' analysis of observational data established that the largest annual variations in depth of the 14°C isotherm occur near 6°N and 12°N . The depth variations at 6°N are found to propagate westward at the speed of a nondispersive baroclinic Rossby wave. The results of Meyers' model correlate well with the observations at 6°N .

In the present model the response of the pycnocline beneath the Countercurrent Trough is a combination of Ekman pumping and a westward propagating Rossby wave. Locally, the depth of the pycnocline is governed by the curl of the wind stress. Wyrtki and Meyers' (1975a) work has shown that the area about 8°N has a mean positive wind stress curl. The upwelling associated with this wind stress curl causes a depth minimum in the meridional profile (Fig. 13).

The annual Rossby wave is generated in response to fluctuations of the wind stress along the eastern boundary. This westward propagating wave has two noticeable effects on the Countercurrent Trough. First, the April to August upwelling signal of the Countercurrent Trough (Fig. 20a) coincides with the period in which the Rossby wave enters the region 140°W - 170°E . Wyrtki and Meyers' maps of wind stress curl also indicate that at 8°N the wind stress curl increases during the March to June period. The presence of the Rossby wave contributes to the wind stress induced upwelling. The Rossby wave also extends the duration of June period. The presence of the Rossby wave contributes to the wind stress induced upwelling. The Rossby wave also extends the duration of the upwelling signal on into August.

The second effect produced by the Rossby wave pertains to the meridional shift of the Countercurrent Trough. The latitudinal location of the Countercurrent Trough (Fig. 23) appears to have a y^{-2} dependency. This is understandable since the phase speed of a nondispersive Rossby wave is a function of y^{-2} . The effect of β on the Rossby wave produces an equatorward shift in the pycnocline depth minimum. This southward displacement of the Countercurrent Trough is in qualitative agreement with Wyrтки's findings.

In this model the total effect of the annual Rossby wave is to alter the location and seasonal variability of the Countercurrent Trough. Since it is the Countercurrent Trough that is being modulated by the Rossby wave, both the North Equatorial Current and the Countercurrent are affected.

Another feature of interest in the eastern half of the basin is distinguished in the zonal velocity field (Fig. 24). At 4°N and 125°W a westward flow is present. The corresponding height field (Fig. 23) demonstrates that this westward flow is generated by the height difference between the Equatorial Ridge and the equator. This driving force is the smaller of the two components that comprise the South Equatorial Current. The majority of the South Equatorial Current flow is due to the height difference between the South Equatorial Ridge and the Equatorial Trough.

The northern component of the South Equatorial Current is separated from the remainder of the current by an eastward flow near the equator. This eastward flow is generated by the meridional pressure gradient from the remainder of the current by an eastward flow near the equator. This eastward flow is generated by the meridional pressure gradient between the equator and the Equatorial Trough. A continuous South

Equatorial Current would result if the Equatorial Trough was located at the equator. In this study the Equatorial Trough is always south of the equator.

There is some observational evidence that confirms the existence of this type of structure in the eastern equatorial Pacific. Tsuchiya (1974) has computed the dynamic topography of the eastern tropical Pacific from February 1967 to April 1968. Data from the EASTROPAC expedition was used to construct seven bimonthly maps of the geopotential anomaly. Several of the maps indicate a westward geostrophic current between the equator and 5°N . Just south of the equator an eastward flow is often present at various longitudes. Tsuchiya states that this current structure corresponds to a displacement of a thermocline ridge (Equatorial Trough) southward from the equator to 1°S - 3°S . Further sources of observational evidence were cited by Tsuchiya.

The last remaining point of interest is the seasonal response of the pycnocline at the equatorial eastern boundary. This pycnocline response to the mean monthly forcing is presented in Fig. 25. There is virtually no comparison between this PHA response and the PHA signal produced by the seasonal harmonics of the equatorial wind stress (Fig. 7).

Since the seasonal harmonics and the MASIG data set were both derived from the Wyrтки and Meyers' wind stress data, one should expect both profiles to be similar. It is evident this is not the case.

One possible explanation for the response at the eastern boundary is that this response may be a combination of both remote and local

One possible explanation for the response at the eastern boundary is that this response may be a combination of both remote and local forcing effects. A brief analysis of the equatorial zonal wind stress

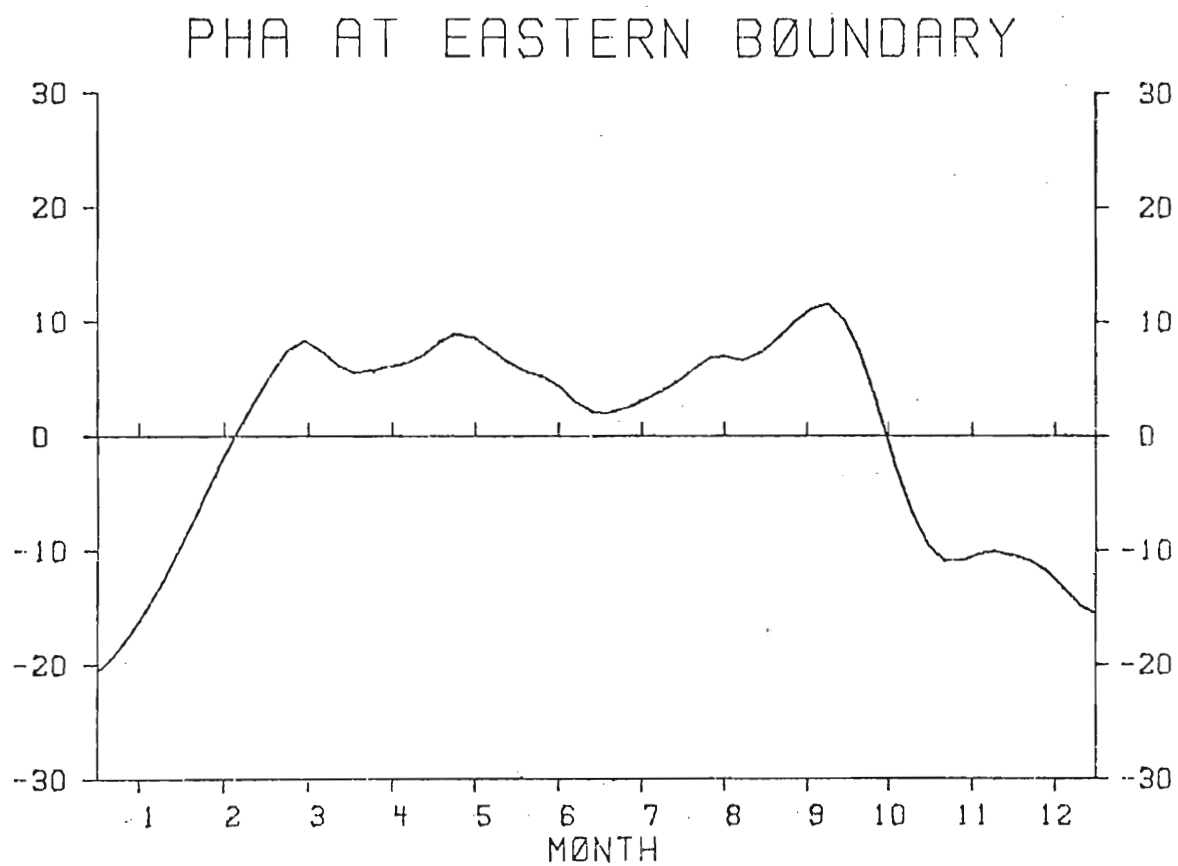


Fig. 25. Pycnocline height anomaly at the equatorial eastern boundary due to forcing of mean monthly wind stresses. Depth variations in meters.

will lend some insight into the problem. The time history of the zonal equatorial wind stress at the eastern boundary (Fig. 26a) has an amplitude more than twice as large as that for the seasonal harmonics between 80°W and 100°W (Fig. 3). The mean annual zonal stress at the eastern boundary is $.02 \text{ N m}^{-2}$ compared with $-.002 \text{ N m}^{-2}$ for the 80°W - 100°W band from Meyers' work. As a result, one main difference between these two eastern boundary PHA responses was the forcing applied near the eastern boundary. When the seasonal harmonics were used as forcing, the eastern boundary region was relatively unforced. When the mean monthly wind stresses were used, there was a definite onshore stress at the boundary.

Even if the effects of local forcing were superimposed upon the remotely forced eastern boundary response in Fig. 7, the large amplitude PHA response between October and March (Fig. 25) cannot be accounted for. Besides the increased stress at the eastern boundary, the amplitude of the interior response differs from that of the seasonal harmonics. The mean monthly zonal wind stress between 160°W and 120°W has been zonally averaged (Fig. 26b) to provide a comparison with the respective signal of the first and second harmonics derived by Meyers. The phase and mean of these two time series are very similar, but the amplitude of the mean monthly stress signal from April to October is larger than that produced by the seasonal harmonics. As discussed in section 3, the PHA response at the unforced eastern boundary is due to remotely forced equatorial waves originating in the interior. Since the phase of the interior mean monthly wind stress is similar to that of the seasonal harmonics, the resulting contribution to the eastern boundary of the interior mean monthly wind stress is similar to that of the seasonal harmonics, the resulting contribution to the eastern boundary response due to remote forcing should have the same phase as the eastern

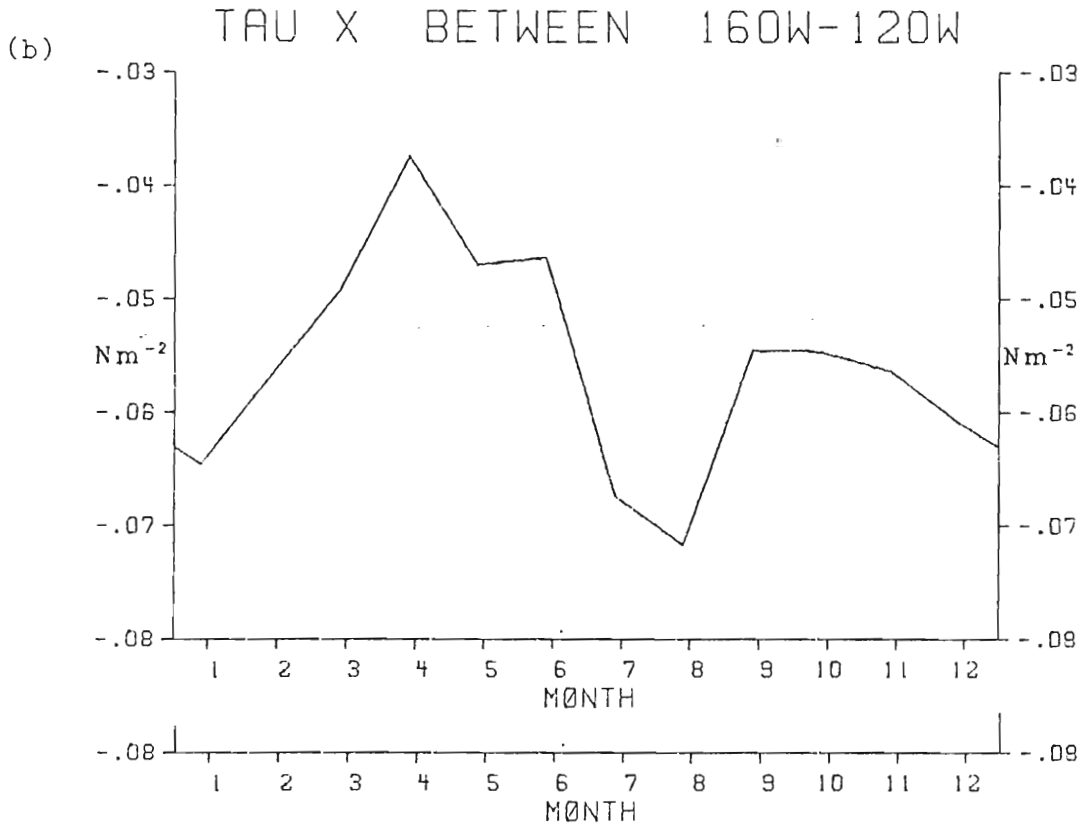
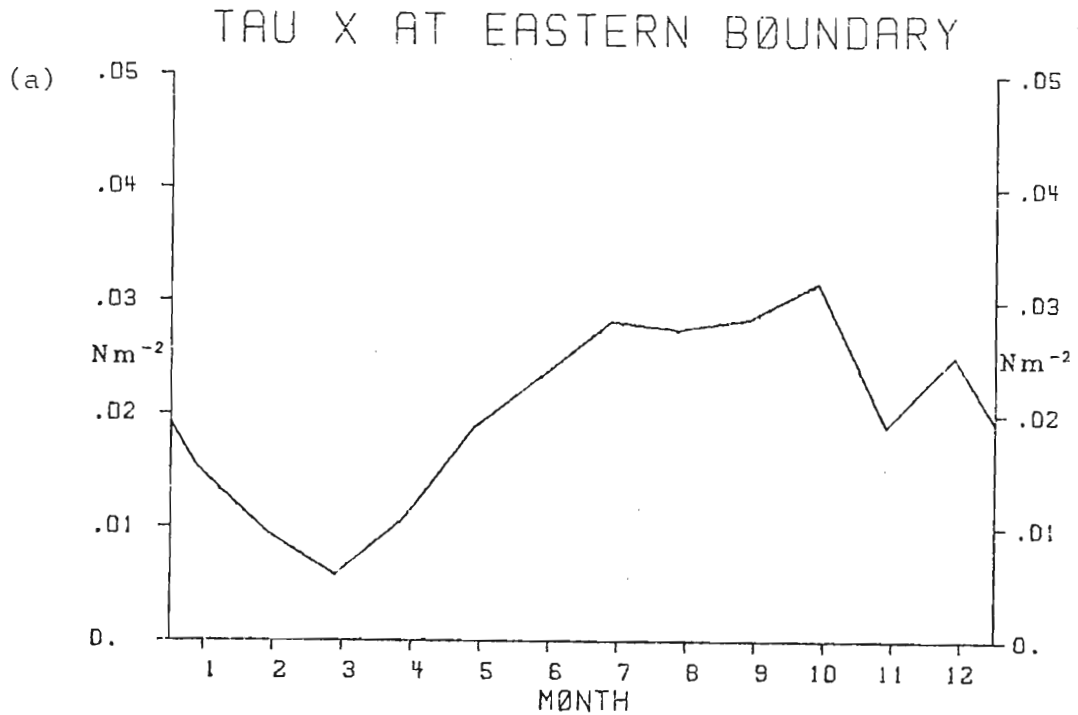


Fig. 26. Zonal equatorial wind stress (a) at the equatorial eastern boundary and (b) averaged between 160°W and 120°W.

boundary response in Fig. 7. The major difference between the remote forcing responses would be a change in amplitude due to the different amplitude of the interior wind stresses. As outlined in Table 1, a combination of local forcing and a revised amplitude remote forcing signal could result in the PHA response at the eastern boundary displayed in Fig. 25. The third column in Table 1 is the predicted contribution to the eastern boundary response due to remote forcing of the mean monthly winds. The amplitude differences between the interior mean monthly winds and the seasonal harmonics were used to predict an increase or decrease in the remotely forced eastern boundary response in Fig. 7.

Since there exists a viable explanation for the eastern boundary response, the final question remaining is: Why doesn't the eastern boundary PHA response agree with observations? When the eastern boundary region was unforced, the agreement between model results and observations was much better. The problem is most likely due to the data set from which the mean monthly wind stresses were derived. Two possible sources of error come to mind. First, the MASIG data set covers a time span of 10 years (1961-1970), or roughly one-half the length of the Wyrтки and Meyers' data set. This subset of wind stress data may have been too short to be fully representative of the period over which the seasonal harmonics of the wind stress and 14°C isotherm depth variations were computed. There is some evidence to support this speculation. Wyrтки (1975) has presented a time series, from 1948 to 1972, of the zonal wind stress over the central equatorial Pacific. Wyrтки (1975) has presented a time series, from 1948 to 1972, of the zonal wind stress over the central equatorial Pacific. Within the band 100°W-140°W a strong annual signal was present from

Wind Stress Stress Seasonal Harmal Harmonics 120°W - 160°W - 160°W	PHA at Eastern Boundary Fig. 7	Predicted PHA at Eastern Boundary due to remote forcing	Mean Monthly Forcing at Eastern Boundary	PHA at Eastern Boundary Fig. 25
January - Apry - April downwelling telling favorable vable	March - June downwelling	March - June downwelling	March - June downwelling favorable	March - June slight downwelling
April - Augus- August upwelling .ling favorable vable	June - September upwelling	June - September increased upwelling	June - September downwelling favorable	June-September slight upwelling
August - Octo - October downwelling elling favorable vable	September - December downwelling	September - December increased downwelling	September - December downwelling upwelling downwelling upwelling favorable	Sept. - January downwelling
October - Janr - January upwelling ling favorable vable	December - March upwelling	December - March decreased upwelling	January - March upwelling favorable	January-March upwelling

Table 1. Remote and local forcing effects at the eastern boundary

1961-1969. The wind stress during the other 16 years had a relatively small or nonexistent annual signal. Consequently, the 10 year MASIG data set is not a representative subset of the 25 year Wyrтки and Meyers data set.

Another source of error could be the subjective analysis of the Wyrтки and Meyers' data. The subjective analysis may have resulted in an overestimation of the wind stress values in the eastern boundary region. This is pure conjecture, but the possibility exists. At the present time the first and second harmonics of the mean monthly zonal equatorial wind stress are being computed so that they may be compared with those computed by Meyers. Furthermore, it would be interesting to know what the eastern boundary response would be if the mean monthly forcing was again applied over the whole basin except for the eastern boundary region. This would eliminate the local forcing contribution, but it would also be cost prohibitive to investigate this singular result.

5. SUMMARY AND CONCLUSIONS

The major goal of this work was to determine if a simple linear model of the tropical Pacific Ocean could reproduce the major features of both the equatorial eastern boundary response and the equatorial current system. This analysis was performed using a linear, one-layer, reduced-gravity transport model on an equatorial β -plane. The coastline geometry of the model basin was an approximation of the tropical Pacific basin from 18°N - 12°S . A non-rectangular model basin was needed because the wind stress used to force the model was based on observations over the non-rectangular Pacific basin. Thermodynamic and thermohaline effects were neglected in the model.

The dynamics present in the model permitted equatorial solutions containing equatorially trapped Kelvin and Rossby waves. The equatorial response included these equatorial waves superimposed upon a zonal balance between the pressure gradient and the wind stress. The extra-equatorial physics allowed for Ekman pumping and the westward propagation of nondispersive Rossby waves. The generation of any meridional pressure gradients resulted in the forcing of zonal geostrophic currents.

The equatorial response, particularly at the eastern boundary was studied along the same lines as Kindle (1979). Annual and semiannual harmonics of the zonal equatorial wind stress calculated by Meyers studied along the same lines as Kindle (1979). Annual and semiannual harmonics of the zonal equatorial wind stress calculated by Meyers

(1979b) were used to force the model. The wind stress was applied in seven longitudinal bands. Each band was 20° wide and the wind stress within each band was constant in x and y . The pycnocline response was then compared with depth observations of the 14°C isotherm.

The east-west slope of the model pycnocline closely approximated the slope of the 14°C isotherm. The pycnocline was displaced downward from its mean depth by 40 meters in the west and was elevated by 70 meters in the east. Along the whole extent of the equator the depth of the pycnocline always fell within a 60 meter thick envelope provided by depth observations of the 14°C isotherm. The major discrepancy between observations and model results occurred near the eastern boundary. It was pointed out that the results could be improved slightly with a better resolution of the wind stress within the 80°W - 100°W band. A more significant change in the mean depth of the pycnocline would result if the wind stress drag coefficient was found to be invalid in this region. The inclusion of a non-constant c^2 in the momentum equation, would also change the mean depth of the pycnocline.

At the eastern boundary a semiannual response was produced remote from any region with a semiannual wind stress signal. The pycnocline response at the eastern boundary was in qualitative agreement with the semiannual displacement of the thermocline. It was also shown that the linear model results were very similar to the linear and nonlinear numerical model results of Kindle. Kindle's models used a rectangular basin but the coastline geometry of the model used in this study approximated the equatorial eastern boundary as a meridional wall. Hence, the linear but the coastline geometry of the model used in this study approximated the equatorial eastern boundary as a meridional wall. Hence, the linear results were similar. Since the linear model results of this study

were comparable to nonlinear results, it was concluded that the equatorial response to wind stress forcing is essentially linear.

An analytical model was used by Kindle to show that the major contributions to the eastern boundary response were from incoming Kelvin waves and first latitudinal mode Rossby waves. The existence of these waves was confirmed in figures of the eastern half of the basin for the model results of this study. These figures displayed the intensification and propagation of these waves as they responded to the wind stress and subsequently generated the eastern boundary response.

The major application of this model was to determine the response of the tropical Pacific to mean monthly winds. The long term mean monthly wind stress was obtained by time averaging the 10 year Mesoscale Air-Sea Interaction Group wind stress data. The MASIG data was the result of subjectively analyzing a 10 year subset of the Wyrтки and Meyers (1975a, b) wind stress data. An advantage of using the MASIG data set was that the Wyrтки and Meyers wind stress data on a 2° latitude by 10° longitude grid was analyzed onto a 2° by 2° mesh.

The response of the model pycnocline to these mean monthly winds produced a meridional profile which resembled the meridional profile of dynamic height presented by Wyrтки (1974a). This pycnocline profile created by the curl of the wind stress, displayed a series of troughs and ridges. The location of these topographic features defined the longitudinal span of the major equatorial surface currents. The height difference across these troughs and ridges geostrophically forced these currents.
difference across these troughs and ridges geostrophically forced these currents.

Of the three major equatorial surface currents, the seasonal variability of the South Equatorial Current was in closest agreement with observations. The strongest flow occurred in March and the weakest in November. The strongest North Equatorial Countercurrent flow occurred in July and November and the weakest flow in March. The seasonal variability of these two currents was out of phase. This phase relation is in agreement with observations of these currents.

The pycnocline response beneath the Countercurrent Trough was found to be a combination of Ekman pumping and an annual, westward propagating Rossby wave. The Rossby wave had the effect of contributing to the upwelling of the pycnocline initiated by the wind stress curl. The y^{-2} dependency of the Rossby wave phase speed resulted in a meridional displacement of the Countercurrent Trough. Wyrтки (1974a) has previously reported that the Countercurrent Trough displays a northward shift of 8°N to 10°N between 170°E and 140°W .

The current structure represented in the model results for the eastern equatorial Pacific was supported by Tsuchiya's (1974) maps of dynamic topography. The model results and dynamic topography maps demonstrated the existence of a westward current just north of the equator separated from the main part of the South Equatorial Current by an eastward current south of the equator. The flow north of the equator was the northern component of the South Equatorial Current. The eastward flow south of the equator was due to the location of the Equatorial Trough south of the equator.

The equatorial eastern boundary responses from the two model applications south of the equator.

The equatorial eastern boundary responses from the two model applications were found to be very different. Further analysis showed that

the eastern boundary response to mean monthly wind stress forcing was a combination of remote and local forcing. A time series of the zonal equatorial wind stress (100°W-140°W) for the 25 year Wyrтки and Meyers wind stress data (Wyrтки, 1975) showed that the 10 year period of the MASIG wind stress data contained an annual signal much stronger than the remaining 15 years. This discrepancy means that the eastern boundary response to the mean monthly winds based on 10 years of wind stress data cannot be compared with the eastern boundary response to the seasonal harmonics based on 25 years of data.

It is recognized that this was a very simple model. Forseeable improvements would be the inclusion of nonlinearities and an increased vertical resolution. Increasing the vertical resolution of the model would allow an analysis of the Equatorial Undercurrent.

The first model application has proved that the equatorial response can be successfully described by a linear model. The results of the second case study have demonstrated that linear dynamics are capable of reproducing the location and variability of the equatorial current system. This study has shown that, to a first order approximation, the upper tropical Pacific Ocean may be modelled by simple linear theory without regard to thermodynamic and thermohaline effects.

APPENDIX

List of Symbols

A	horizontal eddy viscosity coefficient, $10^2 \text{ m}^2 \text{ s}^{-1}$
c	baroclinic phase speed, $(g'H)^{\frac{1}{2}}$, $2. \text{ m s}^{-1}$
g	acceleration due to gravity, 9.8 m s^{-2}
g'	reduced gravity, $g(\rho_2 - \rho_1)/\rho_2$, $.02 \text{ m s}^{-2}$
h	upper layer thickness
H	initial upper layer thickness, 200 m
$\hat{i}, \hat{j}, \hat{k}$	x, y, z-directed unit vectors
t	time
u, v	zonal and meridional components of velocity
U, V	zonal and meridional components of transport
$\vec{\tau}$	total transport vector
x, y, z	tangent plane Cartesian coordinates: x positive eastward, y positive northward and z positive upward
Y	distance from equator to open boundary
β	meridional derivative of Coriolis parameter, $2.25 \times 10^{-11} \text{ m}^{-1} \text{ s}^{-1}$
∇	horizontal gradient operator
∇^2	horizontal Laplacian operator
ρ, ρ_1, ρ_2	densities of seawater
τ^x, τ^y	zonal and meridional components of wind stress, respectively

REFERENCES

- Adamec, D., and J.J. O'Brien, 1978: The seasonal upwelling in the Gulf of Guinea due to remote forcing. J. Phys. Oceanogr., 8, 1050-1060.
- Cane, M.A., 1979a: The response of an equatorial ocean to simple wind stress patterns: I. Model formulation and analytic results. J. Mar. Res., 37, 233-252.
- _____, 1979b: The response of an equatorial ocean to simple wind stress patterns: II. Numerical results. J. Mar. Res., 37, 253-299.
- Charney, J.G., 1955: The generation of ocean currents by wind. J. Mar. Res., 14, 477-498.
- DeWitt, P.W. and A. Leetmaa, 1978: A simple Ekman-type model for predicting thermocline displacements in the tropical Pacific. J. Phys. Oceanogr., 8, 811-817.
- Fedorov, K.N., 1961: Seasonal variations of equatorial currents in the ocean. Problems in Dynamical Oceanography, A.I. Fel'zenbaum, Ed., (Trans., 1968 by Israel Program for Scientific Translations, 183 pp.
- Hellerman, S., 1967: An updated version of wind stress on the world ocean. Mon. Wea. Rev., 95, 607-614 (Corrections, 1968, 96, 63-74).
- Hidaka, K., 1958: Computation of the wind stresses over the ocean. Rec. Oceanogr. Works Japan, 4, No. 2, 77-123.
- Hurlburt, H.E., 1974: The influence of coastline geometry and bottom topography on the eastern ocean circulation. Ph.D. dissertation. Florida State University.
- _____, J.C. Kindle and J.J. O'Brien, 1976: A numerical simulation of the onset of El Niño. J. Phys. Oceanogr., 6, 621-631.
- Kindle, J.C., 1979: Equatorial Pacific Ocean variability--seasonal and El Niño time scales. Ph.D. dissertation. Florida State University.
- Knauss, J.A., 1962: Equatorial current systems. The Sea, Vol. 2, M.N. Hill, Ed., Wiley-Interscience, 235-252.
- Knauss, J.A., 1962: Equatorial current systems. The Sea, Vol. 2, M.N. Hill, Ed., Wiley-Interscience, 235-252.

- Lighthill, M.J., 1969: Dynamic response of the Indian Ocean to onset of the southwest monsoon. Phil. Trans. Roy. Soc. London, A, 265, 45-92.
- Lin, L.B., and H.E. Hurlburt, 1980: Maximum simplification of nonlinear Somali Current dynamics, Monsoon Dynamics, M.J. Lighthill and R.P. Pearce, Eds., Cambridge University Press, (to appear).
- McCreary, J., 1976: Eastern tropical response to changing wind systems: with application to El Niño. J. Phys. Oceanogr., 6, 632-645.
- _____, 1977: Eastern ocean response to changing wind systems. Ph.D. dissertation, University of California, San Diego.
- Meyers, G., 1975: Seasonal variation in transport of the Pacific North Equatorial Current relative to the wind field. J. Phys. Oceanogr., 5, 442-449.
- _____, 1978: Annual variation in the depth of 14°C in the tropical Pacific Ocean. Ph.D. dissertation, University of Hawaii.
- _____, 1979a: On the annual Rossby wave in the tropical North Pacific Ocean. J. Phys. Oceanogr., 9, 663-674.
- _____, 1979b: Annual variation in the slope of the 14°C isotherm along the equator in the Pacific Ocean. J. Phys. Oceanogr., 9, 885-891.
- Moore, D.W., 1968: Planetary-gravity waves in an equatorial ocean. Ph.D. thesis, Harvard University.
- _____, and S.G.H. Philander, 1977: Modeling of the tropical oceanic circulation. The Sea, Vol. 6, E. Goldberg, et al., Eds., Wiley - Interscience, 319-361.
- Munk, W.H., 1950: On the wind-driven ocean circulation. J. Meteor., 7, 79-93.
- O'Brien, J.J., A. Busalacchi and J. Kindle, 1980: Ocean models of El Niño. El Niño and the Peruvian fishery: science, politics and economics, M. Glantz and J.D. Thompson, Eds., Wiley-Interscience (to appear).
- Philander, S.G.H., 1979: Variability of the tropical oceans. Dyn. Atmos. Oceans, 3, 191-208.
- Reid, J.L., Jr., 1961: On the geostrophic flow at the surface of the Pacific Ocean with respect to the 1,000-decibar surface. Tellus, 489-502.
- _____, 1961: On the geostrophic flow at the surface of the Pacific Ocean with respect to the 1,000-decibar surface. Tellus, 489-502.
- Scripps Institution of Oceanography, 1948: The field of mean wind stress over the North Pacific Ocean. Oceanog. Rept. No. 14, 69 pp.

- Stommel, H.M., 1948: The westward intensification of wind-driven ocean currents. Trans. Amer. Geophys. Union, 29, 202-206.
- Sverdrup, H.U., 1947: Wind-driven currents in a baroclinic ocean: with application to the equatorial currents of the eastern Pacific. Proc. Natl. Acad. Sci., 33, 318-326.
- Taft, B.A., and J.H. Jones, 1973: Measurements in the eastern Pacific. Progress in Oceanography, Vol. 6, Pergamon Press, 47-110.
- Tsuchiya, M., 1974: Variation of the surface geostrophic flow in the eastern intertropical Pacific Ocean. Fish. Bull., 72, 1075-1086.
- White, W.B., 1977: Annual forcing of baroclinic Rossby waves in the tropical North Pacific Ocean. J. Phys. Oceanogr., 7, 50-61.
- _____, 1978: A wind-driven model experiment of the seasonal cycle of the main thermocline in the interior midlatitude North Pacific. J. Phys. Oceanogr., 8, 818-824.
- _____, and J.P. McCreary, 1974: Eastern intensification of ocean spin-down: Application to El Niño. J. Phys. Oceanogr., 4, 295-303.
- Wunsch, C., 1977: Response of an equatorial ocean to a periodic monsoon. J. Phys. Oceanogr., 7, 497-511.
- Wyrtki, K., 1974a: Sea level and the seasonal fluctuations in the western Pacific Ocean. J. Phys. Oceanogr., 4, 91-103.
- _____, 1974b: Equatorial currents in the Pacific 1950 to 1970 and their relations to the trade winds. J. Phys. Oceanogr., 4, 372-380.
- _____, 1975: El Niño - The dynamic response of the equatorial Pacific Ocean to atmospheric forcing. J. Phys. Oceanogr., 5, 572-584.
- _____, and G. Meyers, 1975a: The trade wind field over the Pacific Ocean. Part I. The mean field and the mean annual variation. Rep. HIG-75-1, Hawaii Inst. Geophys., University of Hawaii, 26 pp.
- _____, and _____, 1975b: The trade wind field over the Pacific Ocean. Part II. Bimonthly fields of wind stress: 1950 to 1972. Rep. HIG-75-2, Hawaii Inst. Geophys., University of Hawaii, 16 pp.
- _____, and _____, 1976: The trade wind field over the Pacific Ocean. J. Appl. Met., 15, 698-704.
- Yoshida, K., 1955: An example of variations in oceanic circulation in response to the variations in wind field. J. Oceanogr. Soc. Japan, 11, 103-108.
- Yoshida, K., 1955: An example of variations in oceanic circulation in response to the variations in wind field. J. Oceanogr. Soc. Japan, 11, 103-108.